ALMA MATER STUDIORUM - UNIVERSITÀ DI BOLOGNA

ENGINEERING AND ARCHITECTURE SCHOOL

Dipartimento di Ingegneria dell'Energia Elettrica e dell'Informazione "Guglielmo Marconi"- DEI

INGEGNERIA DELL'ENERGIA ELETTRICA
CURRICULUM - ELECTRICAL ENGINEERING

SECOND CYCLE DEGREE DISSERTATION
in
Power Electronic Circuits M

Modular IPT Charging Systems for Drone Applications

Candidate:
Gianluca Gentile

Advisor:
Prof. Vincenzo Cirimele

Co-Advisors:
Prof. Riccardo Mandrioli
Prof. Mattia Ricco

Academic Year 2024/2025
Period I

A chi ne proverà orgoglio,
a mamma Rosalia,
a papà Gianni,
ci stiamo riuscendo.

Provare no. Fare o non fare. Non c'è provare.
Questa è la Via.

ACKNOWLEDGEMENTS

I would like to thank my advisor (for the second time!) Professor Vincenzo Cirimele for his patience, moral support, and essential guidance that allowed me to finish my academic journey with no obstacles. A heartfelt thanks to Professor Riccardo Mandrioli for being the first person to give me trust and for introducing me to the brilliant power electronics research group. Finally, a special thanks to Professor Mattia Ricco for his technical teachings and final rush support.

I would like to express my gratitude to all the members of the power electronics research group who integrated me and made me feel comfortable from day one. I hope our collaboration is just beginning.

Volevo dirvi che sarà mia premura far crescere robusto, il seme della conoscenza che avete instillato in me.

ABSTRACT

This work presents the study, design, and simulation of a modular series-series compensated Inductive Power Transfer system tailored to charging Unmanned Aerial Vehicles, in particular drones used in modern applications. As battery-powered devices, drones face limitations in flight time and operational continuity. Wireless Power Transfer emerges as a promising solution for autonomous and safe energy replenishment. The first part of the work is devoted to providing a general overview of all the components involved in a UAV-WPT network, analyzing the structure and employment of modern drones, the evolution of WPT technologies, and current WPT industry standards (such as WPC Qi). A comprehensive market analysis of drones was carried out to define key electrical and mechanical parameters, guiding the dimensioning of the modular charging system rated at 100-120 W total power, with each module delivering approximately 33 W. Emphasis is placed on the design of coils and magnetic analysis via FEMM of market-ready solutions. The defined Tr30-Re50 with ferrite disk configuration was identified as the best-performing geometry. An interconnected and cooperative environment made up of Plexim PLECS, MathWorks MATLAB and Microsoft Excel was designed and served as the basis for the reasoning and results analysis of a solid 90'000 simulations batch. The built-from-scratch PLECS implementation allowed the evaluation of system behavior, with focus on power transfer and voltage across the load ripple, in different displacement (between the modules) scenarios: no displacement, equal displacement, half-period equal displacement, and random displacement. Another aspect under study has been the quantification of the impact of uncertainties on compensation capacitances. Outcomes highlight the importance of a proper module displacement control strategy and the benefit of frequency shifting to mitigate uncertainty on the component values' impact on the system performance.

Index Terms - Wireless Power Transfer; Inductive Power Transfer; Unmanned Aerial Vehicles; Drone; Modularity; WPT Coil's Design; Market Review; PLECS; Random Displacement; Uncertainty Impact Quantification.

SOMMARIO

Questo lavoro presenta lo studio, la progettazione e la simulazione di un sistema modulare di trasferimento di energia induttivo compensato serie-serie mirato alla ricarica di veicoli aerei senza pilota (UAV), con particolare attenzione ai droni utilizzati per applicazioni reali e moderne. In quanto dispositivi alimentati a batteria, i droni devono affrontare limitazioni nella durata del volo e nella continuità operativa. Il trasferimento di energia senza fili (WPT) emerge come una soluzione promettente per un rifornimento autonomo e sicuro. La prima parte del lavoro è dedicata a fornire una panoramica generale di tutti i componenti coinvolti in un sistema UAV-WPT, analizzando la struttura e l'impiego di droni, l'evoluzione delle tecnologie WPT e gli attuali standard industriali (come il WPC Qi). Una ricerca di mercato sui droni è stata condotta atta a definire i principali parametri elettrici e meccanici, guidando il dimensionamento del sistema di ricarica modulare verso una potenza totale di 100-120 W, con ciascun modulo in grado di processare circa 33 W. Particolare attenzione è posta sulla progettazione delle bobine e sull'analisi delle prestazioni magnetiche tramite FEMM delle soluzioni più promettenti già disponibili sul mercato. La configurazione definita Tr30-Re50 con disco di ferrite è stata identificata come la geometria più performante. È stato realizzato un ambiente interconnesso e cooperativo composto da Plexim PLECS, MathWorks MATLAB e Microsoft Excel, che ha funto da base per il ragionamento e l'analisi dei risultati di un lotto di 90.000 simulazioni. L'implementazione di PLECS ha permesso di valutare il comportamento del sistema, con particolare attenzione al trasferimento di potenza e al ripple sulla tensione ai capi del carico, in diversi scenari di sfasamento (tra i moduli): sfasamento nullo, sfasamento equale, sfasamento equale calcolato su metà periodo e sfasamento stocastico. Un altro aspetto oggetto di studio è stata la quantificazione dell'impatto delle incertezze sulle capacità di compensazione sulle prestazioni del sistema. I risultati evidenziano l'importanza di un'adeguata strategia di controllo dello sfasamento tra i moduli e il vantaggio del cambio di frequenza per mitigare l'impatto dell'incertezza sui valori dei componenti.

Parole chiave - Wireless Power Transfer; Inductive Power Transfer; Unmanned Aerial Vehicles; Drone; Modularità; Progettazione bobine per WPT; Ricerca di mercato; PLECS; Sfasamento stocatisco; Quantificazione dell'impatto dell'incertezza.

Contents

Chapter 1

Introduction to the Work

1.1 Motivation and reference scenario

In today's world, we are experiencing important changes in daily life and productive activities. The fourth industrial revolution is a matter of fact, and the main aspect of the new era is the electrification [1].

With the exponential increase in data collecting, Unmanned Aerial Vehicles (UAVs) have emerged as a promising component of future wireless network infrastructures [2]. The integration of UAVs can significantly enhance both communication performance and energy efficiency, particularly when their mobility and cooperative communication capabilities are effectively coordinated [2]. UAVs have already been deployed across a broad spectrum of applications, including target localization, surveillance, and data acquisition. However, to fully leverage the cooperative and autonomous functionalities of UAV employing systems, it is critical to address and optimize their energy management strategies.

From an energy perspective, UAVs play a dual role. As battery-powered devices, they require the implementation of energy conservation mechanisms to prolong their operational lifespan. Simultaneously, their capacity to carry substantial payloads allows them to function as mobile charging platforms, replenishing the batteries of more resource-constrained devices, including those situated in hard-to-reach environments, such as small-scale Internet of Things (IoT) devices [3]. This dual functionality introduces substantial challenges to energy management in UAV operations. Accordingly, both energy conservation algorithms and dynamic recharging mechanisms must be developed and integrated. Solutions focusing solely on battery capacity management, such as battery replacement or degradation mitigation, may offer temporary relief but often involve high costs and limited practicality [4].

To support continuous UAV operations, energy harvesting approaches utilizing solar or wind energy sources have been investigated. Nonetheless, these methods are constrained by unpredictability and the limited availability of energy over time [3].

In contrast, Wireless Power Transfer (WPT) has gained increasing attention as a more practical and reliable alternative. WPT enables energy to flow without the need for physical connectors, thereby reshaping conventional energy management paradigms across various applications, including opportunity charging for electric automobiles or electric buses and of course, UAVs. Thanks to its inherent flexibility, adjustable positioning, and mobility compatibility, WPT has demonstrated significant potential in powering electric-driven systems.

In a typical WPT-assisted recharging scenario, UAVs receive power from a ground-based charging platform. The UAV can identify and align itself with the charging station using technologies such as wireless communication protocols or advanced image processing algorithms [2]. Conversely, the charging platform may employ sensor-based alignment mechanisms to optimize the spatial configuration between the WPT transmitter and receiver, thereby enhancing the efficiency of the energy transfer process. The focus of this work is the investigation and design of a modular IPT charging system for drone applications.

While current civilian regulations only permit drone operations within visual line-of-sight [5], fully automated UAV-confined missions can be expected in the near future. In this scenario, it will be crucial to implement automated outdoor charging facilities that ensure electrical safety for all devices and living beings. WPT technologies inherently offer these capabilities, making them particularly well-suited for such applications.

1.2 Wireless Power Transfer, a brief overview

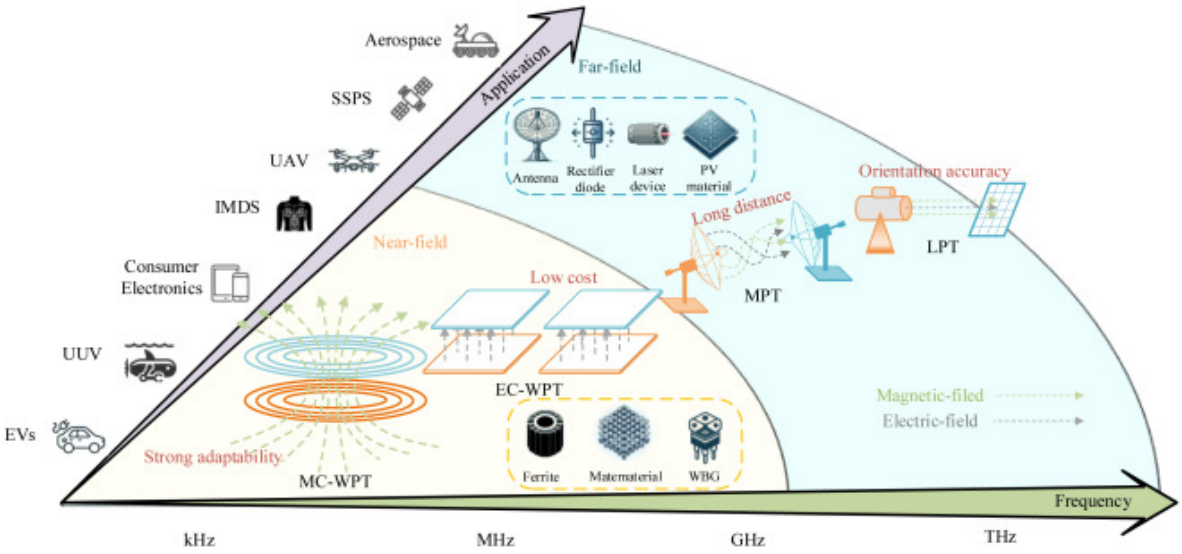

Figure 1.1: Graphical representation of the state of art of WPT technology and its applications. Image retrieved from [6].

In the last decades, the scientific community has indicated all the different mechanisms for the transfer of energy at distance through the generic expression *Wireless Power Transfer* frequently shorten through the acronym WPT. This technology eliminates the need for wires and limits the needed capacity of batteries, enhancing the mobility, convenience, and safety of electric applications. WPT is particularly beneficial for powering electrical devices in scenarios where physically connecting wires is impractical, hazardous, or even impossible.

Among all the possible mechanisms categorized in Figure 1.2 with the main aspects reported in Table 1.1, this work will focus on WPT involving electromagnetic mechanisms, in particular it is dedicated to the *Resonant Inductive Power Transfer* technology.

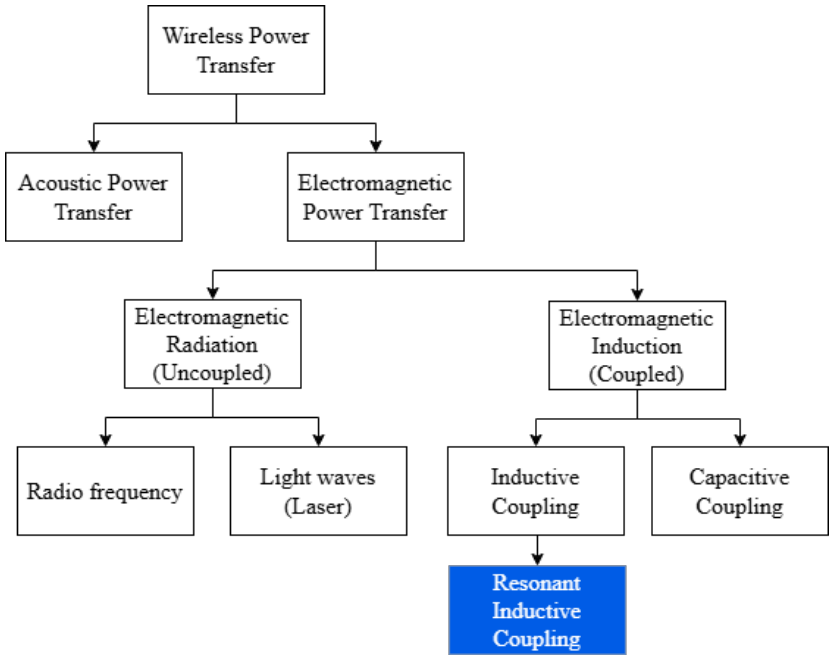

Figure 1.2: Categorization of WPT technologies.

Table 1.1: Baseline characteristics of different WPT technologies [7].

Technology	**Power Transfer**	**Range**	**Frequency**	**Efficiency**
IPT Inductive	W to MW	cm	kHz to MHz	75-95 %
CPT Capacitive	W to kW	mm/cm	kHz to MHz	70-90 %
LPT Laser	W/kW	m/km	THz	40-60 %
RFPT Radio frequency	mW/kW	m/km	MHz to GHz	20-30 %
APT Acoustic	mW/kW	m/cm	kHz to MHz	30-50 %

In most applications of WPT, the system consists of five main parts schematized in Figure 1.3:

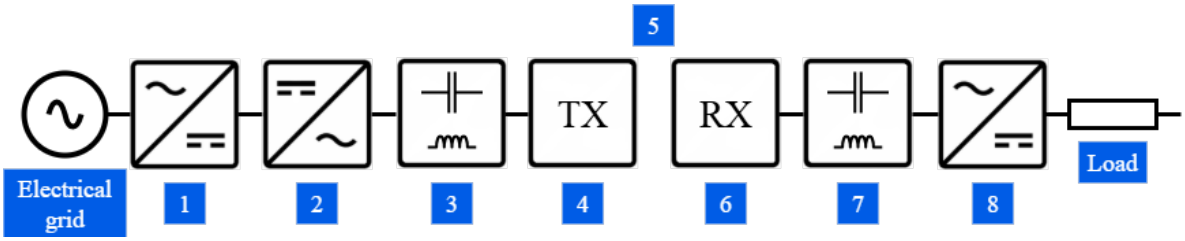

Figure 1.3: Block diagram of WPT generic system.

1. Rectifier device connected to an electrical energy source, most of the time the national electrical grid. The rectifier device could be a diode bridge;

2. Inverter device, so the conversion of a DC current into a well-defined AC current. The amplitude and frequency of the AC power signal depend on the application. Nowadays, the inverter could be a power electronic device such as a MOSFET H-Bridge;

3. Primary compensation network to improve the efficiency of power transfer as explained in Section 2.1;

4. A transmitting coupler to generate a time-varying electromagnetic field;

5. A volume of air in which the electromagnetic field can propagate;

6. A receiving coupler that is surrounded by the electromagnetic field and on which a current is induced;

7. Secondary compensation network, same as point 3;

8. The rectification of the AC current to DC current powering the load.

1.2.1 The evolution of WPT, from Tesla till nowadays

Since the first application of electrical energy, scientists have started to think about a way to transmit this kind of energy in the absence of contacts [8]. The 19th century saw many developments of theories on the transmission of electrical energy. In 1826, André-Marie Ampère discovered a connection between current and magnets. Michael Faraday described in 1832 [9] the induction of an electromotive force driving a current in a conductor loop by a time-varying magnetic flux. At that time, several indications of electrical energy transmission via ether were discovered by many experimenters, but the lack of a coherent theory made it impossible to provide a general overview. After this period of sparkling science, it is possible to start talking about WPT. Four eras of Wireless Power Transfer can be recognized:

The first one is associated with Maxwell and Hertz. Only after the development of Maxwell's equations contained in his *"Treatise on Electricity and Magnetism"*[10], published in 1873, was it possible to establish a theory that unified electricity and magnetism into electromagnetism, predicting the existence of electromagnetic waves as the "wireless" carrier of electromagnetic energy. Then Hertz later experimentally validated Maxwell's equations with his brilliant and ingenious experiments in the 1885-1889 time period.

The second period and the first real improvement in the direction of IPT arrived with Tesla's studies. Tesla invented the expression *Wireless Power Transmission* [11] and demonstrated the first example of transmission without contact at the World Exposition

of Chicago of 1893. In 1900, Tesla patented a system for IPT over long distances (Figure 1.4) using inductors in which he pointed out two important cornerstones of the IPT technology [12]:

1. the necessity to operate at higher frequencies with respect to the ones adopted for other electrical machines;

2. the introduction of capacitors to impose resonance, improving the efficiency of the system.

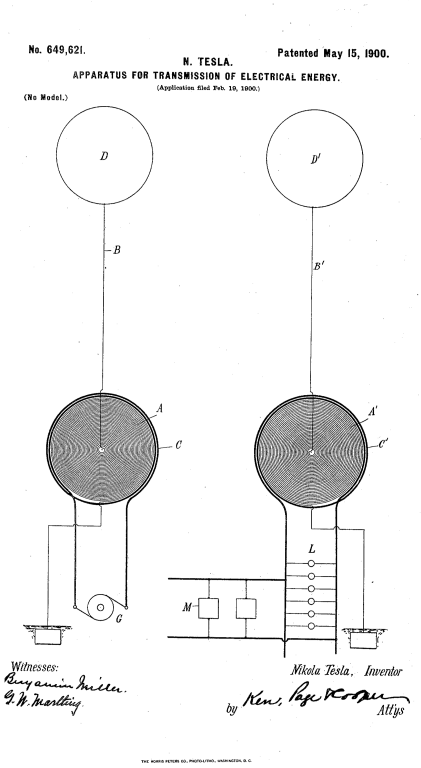

Figure 1.4: First IPT system patented by Nikola Tesla. Illustration extracted from *US Patent 649,621*, May 15 1900 [12].

The third era is represented by the sudden ability acquired during World War II to generate substantial amounts of power at microwave frequencies, where the energy could be focused into a narrow beam with the aid of parabolic reflectors. A significant milestone was achieved with the internationally broadcast demonstration of a microwave-powered helicopter flight at the Spencer Laboratory of the Raytheon Company in October 1964 [8], as illustrated in Figure 1.5. This event not only validated the feasibility of WPT but also highlighted its potential practical application, such as the sustained operation of high-altitude aircraft performing communication and surveillance missions. Such

aircraft could theoretically stay in flight for extended periods by receiving continuous energy transmitted from ground-based stations, thereby eliminating the need for conventional onboard fuel sources.

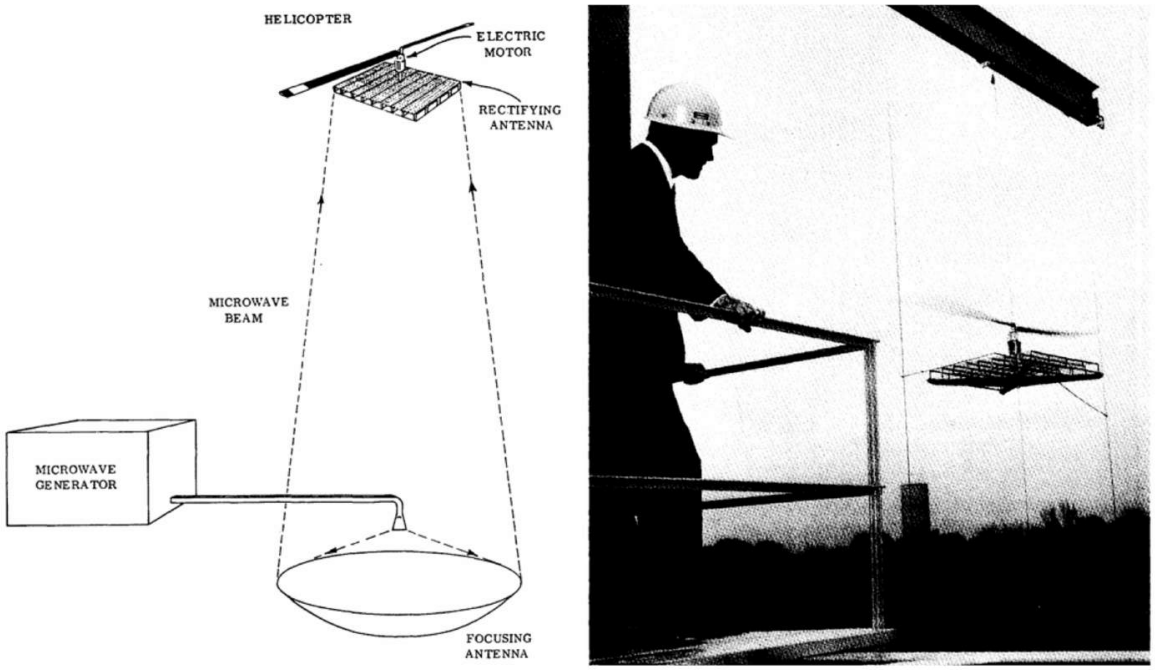

Figure 1.5: Microwave powered helicopter. Schematic and demonstration at the Spencer Laboratory of the Raytheon Company in October 1964. Image retrieved from [8].

The fourth and current period is the commercial and widespread availability of WPT for consumers. The modern applications will be reported in Section 2.1. In particular, this work will focus on the particular application of WPT to drones, reported in Subsection 1.3.3.

1.2.2 Current standardization processes

The standardization of WPT technologies is critical to ensure compatibility, safety, efficiency, and global adoption across different applications. Standards provide clear guidance and frameworks for manufacturers, researchers, and consumers. The following are some of the main WPT standards that play a key role in various fields and applications. Table 1.2 summarizes the scopes of different standards, outlining their relevant characteristics.

- **Qi Standard** [13] from the Wireless Power Consortium. The WPC was established in 2008 and is an open standards development group that works with electronic and technology companies across Europe, Asia and America. The Qi

standard is currently the most widely adopted standard for low-power WPT applications, such as smartphones, wearables, and small electronic devices. The Qi standard focuses on IPT within a few centimeters. Currently, the Qi standard is at the second version, namely Qi v2.0. WPC continues to work on it to improve efficiency, alignment tolerance, and power levels.

- AirFuel Alliance that promotes alternative WPT standards, including: **AirFuel Resonant** [14], based on resonant inductive coupling, which allows multiple device charging, and **AirFuel RF** [15]. The second one is a WPT specification that uses radio frequencies (RF) to enable charging of multiple devices simultaneously within a three-dimensional range, delivering true freedom of movement.

- SAE (Society of Automotive Engineers) International. The **SAE J2954** [16] standard addresses WPT for EVs, focusing on safety, efficiency and EMC. The specification defines three charging levels up to 11 kVA and in future revisions up to 22 kVA. In addition, this standard enables consistent alignment in an exact parking spot, using the Differential Inductive Positioning System (DIPS).

- IEC (International Electrotechnical Commission). As SAE J2954, **IEC 61980** standard addresses WPT for EVs. This standard is divided into three documents: *IEC 61980-1 General requirements* [17], which describes the overall framework, covers architecture, safety, EMC and interoperability. *IEC 61980-2 Communication* [18], specifies the data communication protocols between EV and charging station. *IEC 61980-3 Specific requirements for IPT* [19], including coils alignment, power transfer efficiency and EM field safety.

Table 1.2: Modern WPT standards.

Name	**Technology type**	**Typical application**	**Output power**	**Frequency range**
WPC Qi	Resonant IPT	Smartphones, tablets, small electronics	up to 15 W	110-205 kHz
Airfuel Resonant	Resonant IPT	Laptop, tablets, smartphones	up to 50 W	6.78 MHz
SAE J2954	Resonant IPT	EVs	up to 11 kVA	85 kHz
IEC 61980	Resonant IPT	EVs	up to 11 kVA	85 kHz

1.3 Unmanned Aerial Vehicles, a brief overview

1.3.1 Structure of a modern drone

To fully understand the behavior of a drone is advisable to know what the parts of a modern one are, as well as the characteristics and functions of each one of them. Although there may be some variations from one type of drone to another, some parts are fundamental to the functioning of the system [20].

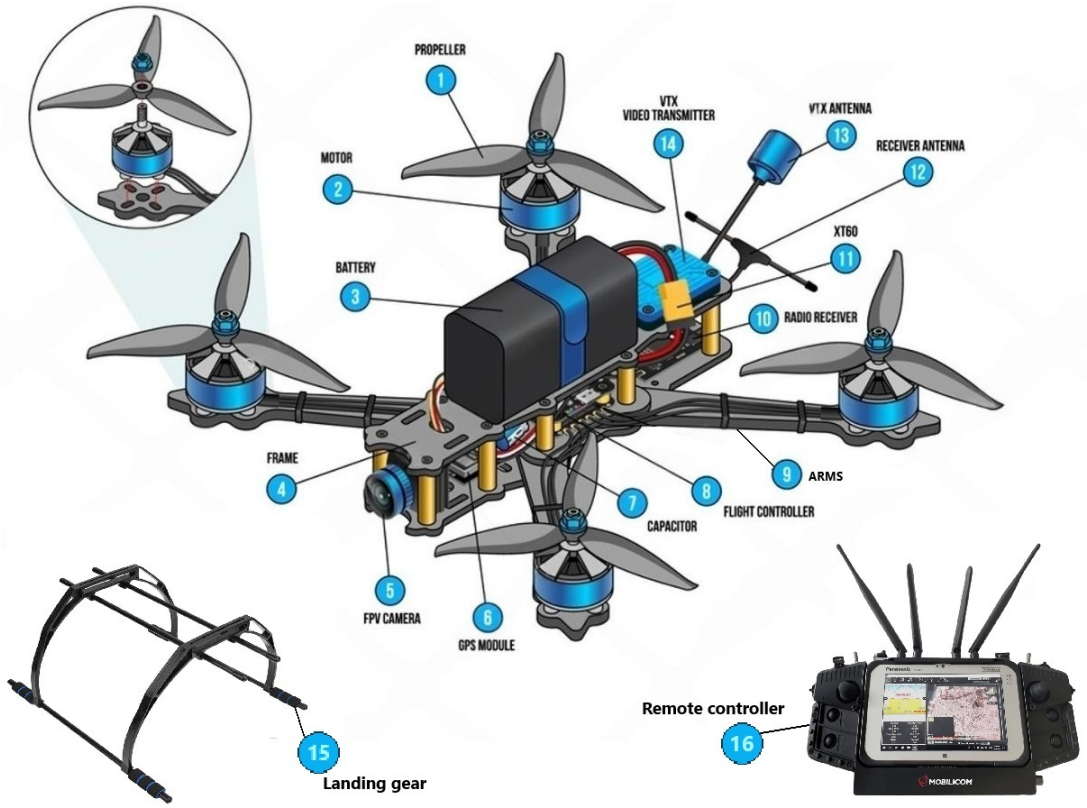

Figure 1.6: Parts of a modern drone. Image adapted from [21].

- **1 - Propellers**, the motors themselves cannot lift the drone, as they must be connected to propellers that are in charge of rotating to provide lift to the drone. Modern drones can be equipped with 4 (quadcopter), 6 (hexacopter), 8 (octocopter), or even more rotors;
- **2 - Motors**, elements of great importance in a drone are the motors. The motors of a drone are located at the ends of each arm of the frame and are responsible for generating the propulsive force for the drone to fly;

- **3 - Battery**, the motors, as well as the other electrical and electronic components of the drone, need power to operate, which they get from a battery that is located in the frame. There are various types of batteries for drones, although the most common are Li-Po batteries, which offer great performance and autonomy in flight. Due to the limited capacity of batteries, the major issue in employing UAVs is the limited time of flight, as shown in Chapter 3;

- **4 - Drone chassis**, the frame or chassis is the main part of a drone and serves the function of holding all the parts together. A perfect chassis would provide high mechanical resistance at the lowest possible weight;

- **5 - Camera**, a professional drone always has a camera (normal or thermal) installed;

- **6 - GPS module**, in case of OLoS or NLoS or loss of communication with the drone, a GPS module is installed to always know where the drone is;

- **8 - Flight Controller Board and sensors**, the FCB is an embedded control system that integrates sensor data acquisition, real-time computation, and actuator control to ensure the dynamic stability, maneuverability, and autonomous operation of the drone. The typical sensors installed are accelerometers, gyroscopes and barometers to estimate the UAV's state (position, orientation, and velocity). Based on these estimations and the control objectives, the FCB generates appropriate actuator signals to modulate the speed of individual motors, thereby achieving precise flight control;

- **9 - Arms**, the arms of a drone are the components that support the motors and are attached to the frame or base structure of the drone. Long arms offer greater stability, while short arms allow for better maneuverability;

- **10, 12, 13, 14 - Communication system**, the listed components are devoted to ensuring the constant communication between the drone and the pilot through the remote controller;

- **15 - Landing gear**, it assures a safe landing on the ground. Further, in case of accessories or suspended load allows to maintain an adequate distance between those and the landing terrain;

- **16 - Remote controller**, the remote controller is the device that directly connects the drone and the pilot. It is generally composed of analog sticks and digital buttons. In case of an installed camera on the drone a touchscreen monitor is embedded.

1.3.2 What material is a drone made of?

The selection of materials used in the fabrication of drone components is a critical factor influencing the overall flight performance and operational efficiency of the UAV. Each component must be manufactured from materials that are not only lightweight but also exhibit high mechanical strength and impact resistance to ensure durability under various operating conditions. Typically, materials such as high-grade plastics and carbon fiber composites [20] are employed to minimize the drone's total mass while maintaining structural integrity. Among these, carbon fiber has emerged as a preferred material in drone manufacturing due to its exceptional strength-to-weight ratio. Its superior mechanical properties make it particularly suitable for constructing the primary structural elements of drones, including the frame and support structures, thereby enhancing both the robustness and maneuverability of the platform. Materials considerations are the central aspect of the Chapter 4.

1.3.3 Modern employ of drones

The use of UAVs opens up new and efficient ways to resolve complex problems. In the following, practical and specific drone application areas are listed [20]:

Figure 1.7: Real-world emergency applications of drones.

- Emergency response and rescue missions. When disaster strikes, the priority is to save lives. During an emergency, the sudden action of first responders could mark the difference between life and death. Another crucial aspect is not to put the rescuer's incolumity in danger by forcing not safe actions. In this scenario, the

deployment of UAVs is leading the new frontier of emergency response. They can be used to quickly assess the situation, locate victims, and even deliver supplies and aid. Drones equipped with normal and thermal cameras provide a bird's eye view of the situation, minimizing the risk to emergency responders by allowing remote operation from almost anywhere;

- Forest fire detection and monitoring. This dramatic event, in addition to causing economic damage and danger to life, has serious ecological and environmental consequences, with negative repercussions on all elements of the ecosystem, including long-term ones such as drought, desertification and hydro-geological instability. The possibility of suddenly identifying the ignition zone and monitoring the spreading could avoid the worst;

- Structural inspections (bridges, skyscrapers, historical monuments, PV plants [22] and overhead power lines [23]);

- Road patrol. In the sector of transportation and traffic management, a fleet of UAVs can reduce the cost and improve the effectiveness of action in an urban scenario;

Figure 1.8: Other real-world applications of drones.

- Modern agriculture and farming. The exploitation of the soil for feeding is one of the pillars of the development of humanity. Over the centuries, these activities have evolved and nowadays the presence of sensors and active monitoring enables efficient use of resources. One example of *precise agriculture* is reported in [24];

- Oil and gas site monitoring [25]. Spilling of oil and gas leaks are a danger to life, environmental and economical problems.
- Light shows and drone swarms, for entertainment and cultural purposes;
- Last-mile delivery (e.g. medications and consumer goods). The use of drones for delivery is becoming common in urban contexts. Such as e-commerce for instant delivery or medical assistance for the delivery of uncommon drugs.

Chapter 2

Wireless Power Transfer Basics

2.1 Introduction to Wireless Power Transfer

Wireless Power Transfer (WPT) refers to a technology that enables the transfer of electrical energy from a power source to a power receiver without the need for physical connection. As discussed in Subsection 1.2, nowadays, the two main utilized technologies are Resonant Inductive Power Transfer (IPT) and Resonant Capacitive Power Transfer (CPT), which will be deeply explained in this chapter. As a matter of fact, IPT is more widely studied and implemented in commercial applications than CPT, anyway due to some important advantages, the interest in CPT has rapidly grown in recent years. WPT is continuously advancing, allowing for increased power transfer, efficiency, longer distances, and larger-scale deployments. It is becoming a fundamental way to exchange power between systems. As WPT evolves, new possibilities and applications are emerging, just to name a few modern ones, the powering and charging of: Electric vehicles (EVs), medical implants, consumer electronics such as smartphones, smartwatches, electric toothbrushes, etc..., industrial automation and robotics, Unmanned Aerial Vehicles (UAVs) such as drones, Internet of Things (IoT) devices and Wireless Sensor Networks (WSNs). WPT offers several important benefits that make it an interesting solution for modern applications [7]:

- It removes the hassle of physical connectors and cables, so connecting wires to the devices. As a result, it eliminates the need for an operator. This is a perfect feature for the charging of autonomous drones;
- WPT devices do not need an open connector slot for charging, so an entirely sealed device is possible. By doing so, the resistance to water and dust intrusion is significantly increased;
- Eliminating physical connectors results in increased durability of devices; Furthermore, it prevents damage to devices due to incorrect or forceful plugging.

The implementation of WPT brings to the table some disadvantages [7] as well:

- Wireless charging infrastructure requires a significant implementation cost;
- Higher power losses, so lower efficiency compared to a wired solution;
- Limited range, generally within a few centimeters to a few meters. Further, the transmission efficiency rapidly decreases with increasing distance;
- Electromagnetic compatibility (EMC) with neighboring devices has to be counted;
- Electric and magnetic fields (EMF) exposure has to be taken into consideration for safety;
- WPT is limited to lower power exchange compared to a wired solution.

2.2 IPT - Inductive Power Transfer

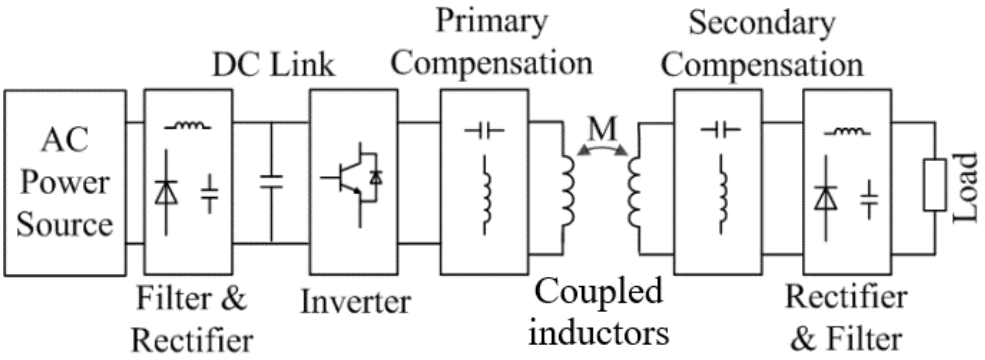

Figure 2.1: Block diagram of IPT generic system. Image retrieved from [26].

An IPT system employs a magnetic field to transfer power. The system is composed of two main parts, the transmitter and the receiver. The AC power source (commonly the national electrical grid) is first filtered and rectified (generally by a diode full-wave rectifier) to make available a DC power source for employing the inverter (nowadays could be a SiC FET H-Bridge). Then comes the actual transmission system, both the transmitter and receiver include a coil and a compensation circuit. The receiver coil is designed to be coupled with the transmitter coil, resulting in a mutual inductance. The coils often require litz wire to be assembled along with a proper shielding ferrite base. Regarding the compensation circuits, the four basic compensation topologies employing only capacitances are shown in Figure 2.2. In addition, it is possible to use both capacitances and additional inductances, resulting in hybrid compensation schemes such as LCL (inductance-capacitance-inductance) or LCC

(inductance-capacitance-capacitance). After the receiver compensation circuit comes another rectifier, then a filter to permit the powering of the load.

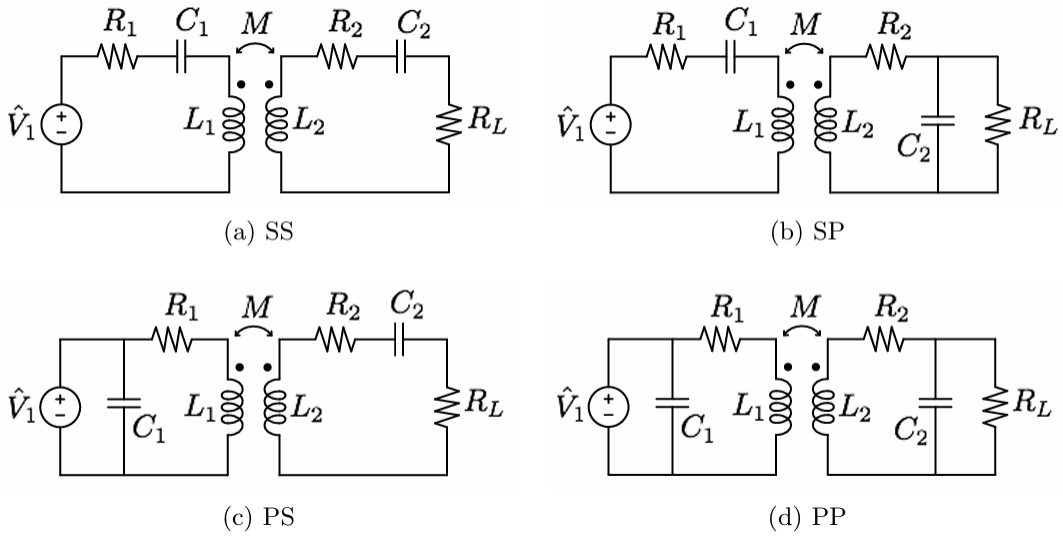

Figure 2.2: Circuit representation of the four basic compensation topologies. Image retrieved from [27].

Here is a brief explanation of how the system works: Retrieving energy from the grid. Transmitter coil is energized by a high-frequency AC voltage generated by the inverter, resulting in an oscillating magnetic field. The receiver coil is immersed in it, so an alternating voltage is induced on the receiver coil, which makes an alternating current flow. This current is then rectified and filtered and used to power the load.

2.2.1 Focus on series-series compensated IPT

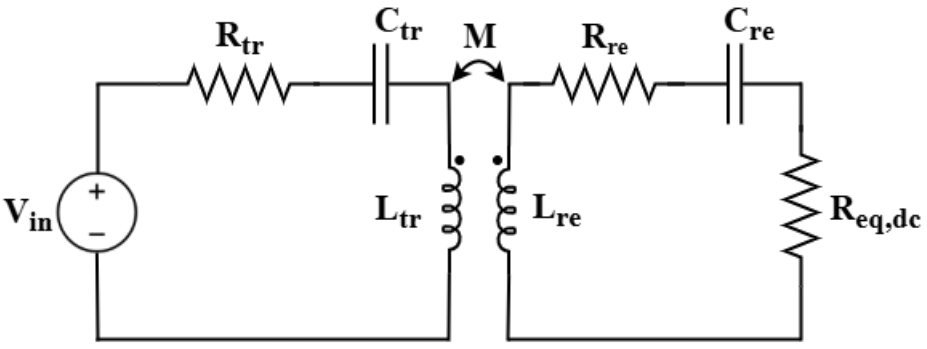

Figure 2.3: Circuit representation of the series-series compensation topology.

Series-series compensated IPT is based on installing compensation capacitances in series with both the transmitter and receiver coils. The values of the series capacitances are chosen to resonate with the self-inductance of the coils at the operating frequency,

resulting in a resonant circuit on both sides. This configuration creates a narrow-band resonant system that enhances power transfer at a specific frequency. The resonance condition occurs when the inductive reactance and capacitive reactance cancel each other:

$$\omega^2 L_{tr} C_{tr} = 1,\ \omega^2 L_{re} C_{re} = 1 \tag{2.1}$$

Among the compensation schemes presented in Section 2.2, the SS-IPT was chosen due to the following reasons:

- The system is not very sensitive to misalignment [28].
- The resonance frequency does not depend neither on the load (optimum because the internal resistance of a battery changes with the SoC) nor on the coupling between transmitter and receiver. These aspects are confirmed by the resonance condition 2.1. This expression changes for the other compensation topologies.
- When properly designed, the system provides constant current output despite load variations, which simplifies current regulation. This behavior makes it suitable for current-regulated applications (e.g., battery charging) [28].

The calculation expressions of all the parameters for the SS-IPT are reported in Appendix A.

2.3 CPT - Capacitive Power Transfer

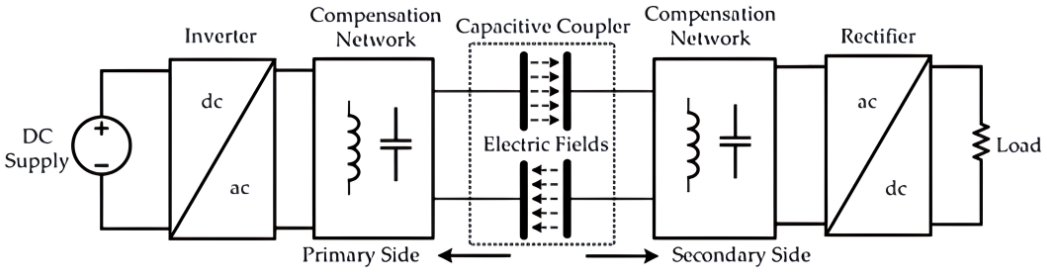

Figure 2.4: Block diagram of CPT generic system. Image retrieved from [29].

As explained in Section 1.2, the other electromagnetic induction WPT technology is the capacitive power transfer. A CPT system employs an electric field to transfer power. The only conceptual difference with a resonant IPT system is the capacitive coupler that takes the place of the inductive coupler. It works by using the capacitance of a dielectric material, usually air, to create a conductive path between two circuits. The capacitive coupler is usually composed of four metal plates (for instance, aluminum)

required in a CPT system to draw a closed circuit where current can flow. Two plates are used on the primary side as the transmitter and the other two on the secondary side as the receiver. The design of the capacitive coupler aims to reach the highest mutual capacitance and reduce the misalignment between the transmitter and receiver.

The main problem of a CPT system is that the achievable mutual coupling capacitance, which determines the power transfer, due to the vacuum permittivity $\epsilon_0 \simeq 8.85 \cdot 10^{-12}$ F/m (compared to the vacuum permeability $\mu_0 \simeq 12.6 \cdot 10^{-7}$ H/m), is relatively low (from tens pF to hundreds pF) [30]; This aspect is directly recognizable from the capacitance expression of a generic capacitor:

$$C = \epsilon_0 \epsilon_r \frac{S}{d} \tag{2.2}$$

Where ϵ_0 is vacuum permittivity, ϵ_r is the relative permittivity of the substance between the plates, S is the area of the armatures, and d is the distance between them.

This leads to high impedance so the need to work at relatively high frequency (100's kHz to 10's MHz) [31][30] and of a proper compensation network. This translates to a lower power density compared to IPT.

Chapter 3

Modern Drones' Research

3.1 Drone classification and market review

Drones come in a vast variety of sizes and configurations, from small and light quadcopters used for recreational purposes to large and complex eight-rotor drones used for the professional purposes listed in Subsection 1.3.3. Modern drones are often equipped with cameras, sensors, and other instruments that allow them to collect data and perform specific tasks. Despite their many advantages, drones also raise concerns about safety, privacy, and security. In response, regulatory agencies around the world have developed rules and guidelines governing the operation of UAVs in different environments, including restrictions on where and how they can be flown, and requirements for licensing and registration.

This chapter aims to summarize the investigation of the main commercial brands **DJI** [32] **Parrot** [33] **FreeFly** [34] **FIMI** [35] and **Yuneec** [36], resulting in the collection of data regarding electrical and mechanical quantities.

According to the proposed drones' categorization by Zakora and Molodchik [37] based on weight and flight range, in Table 3.1, the main features of 25 drones available on the market categorized as **Mini and Micro UAVs close range** and **Lightweight UAVs small range** are collected.
Overcoming the proposed categorization, *Mini* and *Micro* classes will be split into two, resulting in 3 weight groups:

- Super light drones, up to 800 grams. This category is composed of drones for entertainment purposes;
- Medium drones, from 800 to 5000 grams. These aircraft are widely applicable, from racing drones to aid for emergency services;
- Heavy drones, over 5000 grams. Typically employed for the professional purposes listed in Subsection 1.3.3.

Table 3.1: Review of the drone market.

Brand	Name	n. rotor	Drone weight [g]	Dimension [mm]	Volume [cm3]	Chassis (main) material	Battery technology	Bat. Capacity [mAh]	Bat. Voltage [V]	Other Bat. Info	Max charging power [W]	Bat. Energy [Wh]	Bat. Weight [g]	Battery Energy density [Wh/kg]	Bat. weight % on total drone weight	Declared time of flight - No Payload [min]	C-rate (discharge)	C-rate (charge)	Camera
DJI	Mavic Mini 2	4	242	245×289×56	3965.1	Plastic	LiPo 2S	2250	7.7	Max charging voltage: 8.8 V; Max charging power: 29 W	29.0	17.3	86	200.9	36%	31		1.67	4K 12 MP
DJI	Avata	4	410	180×180×80	2592.0	Plastic	Li-ion	2420	14.8	Max charging voltage: 17 V; Charging power: 65 W;	65.0	35.7	162	220.4	40%	18	7C	1.82	48 MP
Parrot	ANAFI USA	4	496	282x373x84	8835.6	Carbon fiber	3 x LiPo (cell 4.4V)	3400	13.2	Max charging power: 30 W Charging time: 112 min	30.0	44.9	195		39%	32		0.67	Thermal: -40 °C to +150 °C
FIMI	A3 Drone	4	560	285x229x69	4503.3	Plastic	3xLi-Po	2000	11.1	Max charging power: 20 W; Charging time: 70 min; Max charging voltage: 12.75 V;	20.0	22.2	162	137.0	29%	25		0.90	
DJI	Mavic Air 2	4	570	183×253×77	3565.0		LiPo 3S	3500	11.6	Max charging voltage: 13.2 V; Charging power: 65 W;	65.0	40.4	198	204.1	35%	34		1.61	48 MP
FIMI	X8SE 2020	4	765	204x106x72,6	1569.9	Plastic	Li-Po 3S	4500	11.4	Max charging voltage: 13.05 V;		51.3	270	190.0	35%	35			48 MP
DJI	FPV	4	795	255×312×127	10104.1	Plastic	LiPo 6S	2000	22.2	Max charging voltage: 25.2 V; Max charging power: 90 W	90.0	44.4	295	150.5	37%	20	10C	2.03	
DJI	Mavic 3	4	895	347.5×283×107.7	10591.5	Plastic	Li-ion 4S	5000	15.4	Max charging voltage: 17.6 V; Charging power: 65 W; Charging time: 96 min;	65.0	77.0	336	229.5	37%	46		0.84	20 MP
Parrot	ANAFI Ai	4	898	320x440x118	16614.4		3 x LiPo (cell 4.4V)	6800	13.2	Max charging power: 45 W	45.0	89.8	366		41%	32		0.50	4K UHD 48 MP
DJI	Phantom 4 Pro V2	4	1375	392×328×222	28543.9	Plastic	LiPo 4S	5870	15.2	Max charging power: 160 W	160.0	89.2	468	190.6	34%	30		1.79	20 MP
FIMI	Mi Drone 4K	4	1450			Plastic	LiPo 4S	5100	15.2	Max charging voltage: 17.4 V; Charging current: 2.9 A; Charging power: 49.3 W;	49.3	77.5	450	172.3	31%	26		0.57	
Yuneec	Typhoon H520	6	1645	520x457x309	73430.8	Carbon Fiber	LiPo 4S	5250	15.2	Charging time: 120 min; Charging current: 3.15 A;	47.9	79.8				27		0.60	
Yuneec	Typhoon H3	6	1985				LiPo 4S	5250	15.2	Charging time: 120 min; Charging current: 3.15 A;	47.9	79.8				25		0.60	
DJI	Inspire 2	4	3440			Carbon fiber	LiPo 6S	4280	22.8	Max charging power: 180 W	180.0	97.6	1030	94.7	30%	25		1.84	
DJI	S800 EVO	6	3700	460×425×320	62560.0	Carbon fiber	LiPo 6S	12000	22.2	ESC current: 40A; Max power consumption: 3 kW		266.4				20	15C		
DJI	S1000	8	4200	460×511×305	71693.3	Carbon fiber	LiPo 6S	15000	22.2			333.0				15	15C		
DJI	Matrice 200 V2	4	4690	883×886×398	311370.5		TB55 (LiPo 6S)	15320	22.8	Charging voltage: 26.1 V; Charging power: 180 W;	180.0	349.3	1770	197.3	38%	38		0.52	
Freefly	Astro	4	5165	1407x359x1407	710694.0	Carbon fiber, Plastic	SL8 - Air x 2 (LiPo 6S)	14600	22.2	Charging power: 200 W; Single Motor max continuos power output: 350 A;	200.0	314.0	2070	151.7	40%	37		0.62	
DJI	Matrice 300 RTK	4	6300	810×670×430	233361.0	Carbon fiber	TB60 (LiPo 12S)	11870	44.4	Charging time: 60 min; Charging current: 14.244 A;	632.4	527.0	2700	195.2	43%	55		1.20	Video 960p
DJI	Matrice 600 Pro	6	10000	1668×1518×727	1840781.4	Carbon fiber	TB48S (LiPo 6S)	34200	22.2	Max charging power: 180 W	180.0	759.2	4080	186.1	41%	38		0.24	
Freefly	Alta 8 Pro	8	10400	1720x360x1720	1065024.0		LiPo 12S	14700	44.4	Single Motor max continuos power output: 100 W;		652.7				34	0.61		
Freefly	Alta X	4	10860	2273x387x2273	1999446.7		LiPo 12S	32000	44.4			1420.8				47	20C		
DJI	MG-1P	8	13700	1460×1460×578	1232064.8	Carbon fiber	MG-12000P (LiPo 12S)	12000	44.4	Max charging power: 1200 W	1200.0	532.0	4000	133.0	29%	25	20C	2.25	
DJI	Agras T16	6	24500	2509×2213×732	4064369.2		AB2	17500	51.8			906.0	6000	151.0	24%	24			
DJI	Agras T20	6	27500	2509×2213×732	4064369.2		AB3	18000	51.8			932.4	6400	145.7	23%	20	9C		

As a result of the market review reported in Table 3.1, independently of the category, all drones have similar characteristics:

- As shown in Figure 3.1, in changing the capacity of the battery, the percentual weight on the total oscillates from 30% to 40%. The percentage tends to decrease to 25% in increasing the total weight of the drone;

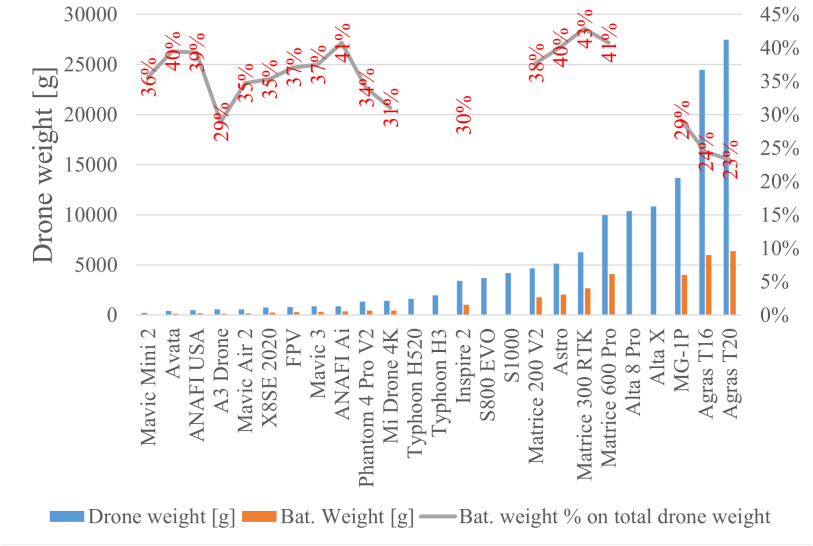

Figure 3.1: Drone weight versus onboard battery weight.

- The declared time of flight is low, from 20 to 55 minutes. As shown in Figure 3.2, reporting the data of the research, a correlation index of 0.476 is calculated, so a good dependence of the battery energy density on the flight time can be recognized;

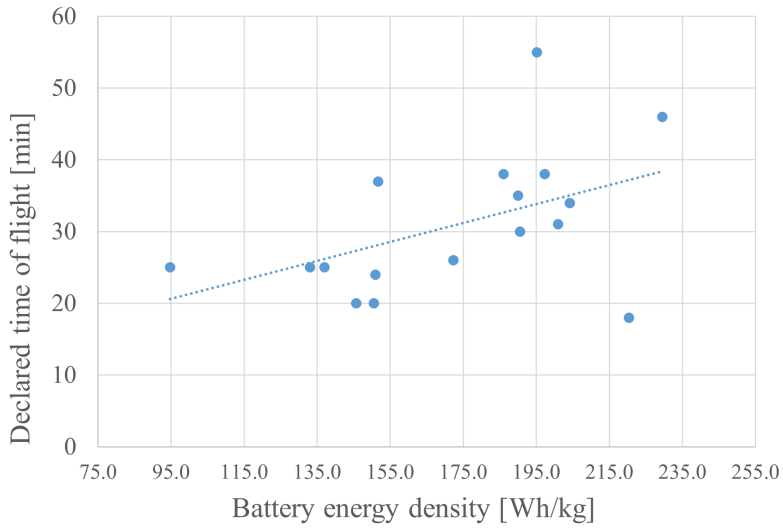

Figure 3.2: Battery energy density versus declared time of flight.

- Energy density of the battery lies in the range 130-210 Wh/kg;
- Charging C-rate is always below 2.5;
- The commonly used battery technology is Li-Po or Li-Ion;
- Have a high-quality camera;
- The batteries' voltage is sharply different, and a mild trend of increasing voltage with increasing weight can be recognized in Figure 3.3.

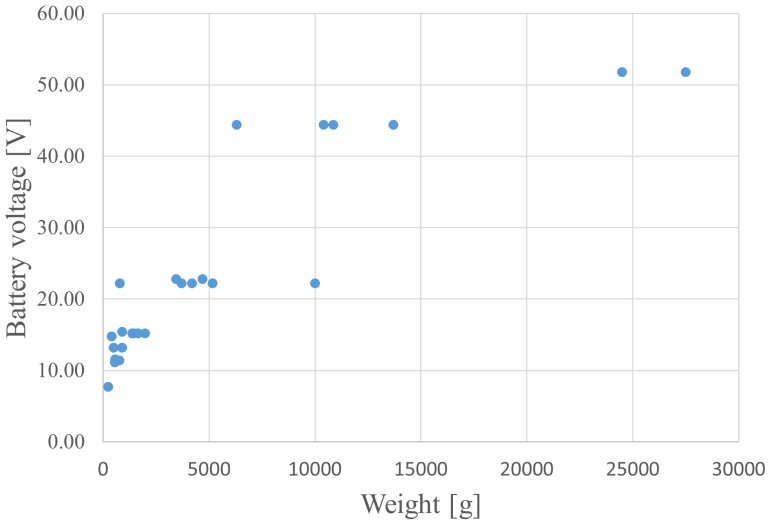

Figure 3.3: Battery voltage versus drone weight.

3.2 Sky Hero Spy Y6

Particular attention is paid to the Sky Hero Spy Y6 drone, visible in Figure 3.4. This drone weighs 780 grams without the battery pack. The drone frame is made of nylon-reinforced carbon fiber and rests on gearing consisting of two tubular rods inclined 65° to the ground each one attached via a plastic clamp to a second tubular rod arranged horizontally. Normally, a 6300 mAh battery having a nominal voltage of 22.2 V is installed. This drone will be used as reference for the study conducted in Chapter 4.

Figure 3.4: Actual Sky Hero Spy Y6 photo. Image retrieved from [38].

3.3 Summary of drone classes

3.3.1 Super light drones

This category of drones is characterized by a plastic chassis and 4 rotors. Their usage is limited to entertainment purposes and cannot withstand strong winds and severe weather (Parrot Anafi USA makes an exception). The battery voltage goes from 7.7 V to 11.4 V.

3.3.2 Medium drones

This category of drones is the most heterogeneous, characterized by plastic and carbon fiber chassis and a number of rotors from 4 to 8. Their usage is wide, from racing to filming to emergency services. They can withstand severe weather, high temperatures, and singular environments. The battery voltage goes from 13.2 V to 22.8 V.

3.3.3 Heavy drones

Due to the high weight, this category of drones is characterized by carbon fiber chassis and has from 4 to 8 rotors. Their usage is for professional purposes only. The battery voltage goes from 22.8 V to 51.8 V.

Chapter 4

Design Considerations on Modular WPT Charging Systems for Drones Applications

To demonstrate a commitment to best practices, guarantee interoperability with other commercial solutions, and assure compliance with regulations, the Qi standard (presented in Subsection 1.2.2) will be followed for the next design decisions. As a result of the market review, focusing on medium and heavy drones, a typical voltage of 24 V is assumed for the battery at full charge. Although batteries for drone applications have very high discharge C-rates, it is generally recommended to use a charging C-rate as close as possible to 1C. Therefore, the goal of this writing is to make a charging system that works with such a C-rate and thus with a power in the range 100-120 W. As cited in Subsection 1.2.2, this power level is not contemplated in the Qi v2.0. Hence, to overcome this limitation, a modular approach is proposed. The approach consists of thinking of the overall charging system as a system composed of modules that individually handle a power compatible with the Qi indications. Then all the modules are connected in parallel to achieve the desired total output power. A clear representation of the concept of modularity is reported in Figure 4.1.

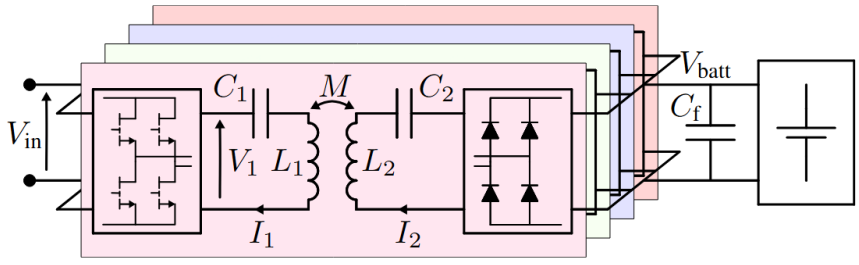

Figure 4.1: Representation of the concept of modularity. In the scheme is also represented the output filter capacitance C_f that will be the last topic covered. Image retrieved from [38].

Another important advantage of the modular approach is the reduction in the current managed by a single module. Consequently, the attention is moved toward the adoption of GaN transistors, allowing to operate at the upper end of the frequency range indicated by the Qi v2.0, that is 205 kHz as indicated in Table 1.2. Finally, each coil pair is designed to handle a rated power of 33 W, which is a value close to the current limit prescribed by the Qi v2.0.

Again, Qi v2.0 indicates that the maximum radius for a coil is 50 mm. Focusing on the structure of the reference drone 3.4, two installation points can accommodate the receiving coil. On the central part of the landing gear or at one end of the horizontal tube. These mounting positions yield sufficient space between the coils to neglect mutual magnetic coupling, so each module can be studied independently.

The above evaluations are summarized in Table 4.1. A litz wire having a diameter of 1 mm will be used for all coils. This assures a low current density (around 2 A/mm^2), so a safe operation regarding thermal dissipation with natural convection cooling.

Table 4.1: Requirements of the single module under development.

Parameter	**Symbol**	**Value**
Rated power per phase	P_{SMO}	33 W
Rated input voltage	V_{in}	24 V
Rated output voltage	V_{out}	24 V
Rated transmitter coil current (RMS)	I_{tr}	1.53 A
Rated receiver coil current (RMS)	I_{re}	1.53 A
Working frequency	f	205 kHz
Target mutual inductance	M_t	11 µH
Air-gap	-	10 mm

4.1 Coil design

The coil design is based on the evaluations and procedures described in [39] and [40]. From the work [39], setting the desired power to be transferred, target value of mutual inductance is calculated considering the output of the inverter feeding the transmitting coil a square wave of amplitude V_{in} and a voltage at the output of the rectifier equal to the battery voltage V_{out}. In this situation, it is assumed to transfer the nominal power P_{SMO}. The target value of mutual inductance between the coils is given by:

$$M_t = \frac{8}{\pi^2} \frac{V_{in} \cdot V_{out}}{\omega_0 \cdot P_{SMO}} \tag{4.1}$$

The coefficient $8/\pi^2$ is derived from representing the load under nominal conditions by an equivalent resistor of value $R_{eq,dc} = V_{out}^2/P_{SMO}$ brought back upstream of the rectifier [27], namely:

$$R_{eq,ac} = \frac{8}{\pi^2}\frac{V_{out}^2}{P_{SMO}} = \frac{8}{\pi^2}R_{eq,dc} \tag{4.2}$$

Given the target value of M_t, there are countless combinations of coils' number of turns and coil areas for obtaining it. To guarantee the controllability of the system and to avoid the so-called bifurcation (explained in Subsection 5.2.1), as stated in [40], it is necessary to ensure that the transmitter quality factor Q_{tr} is higher than the receiver's one Q_{re}. These parameters are defined as

$$Q_{tr} = \frac{R_{eq,ac} \cdot L_{tr}}{\omega_0 \cdot M^2}, \quad Q_{re} = \frac{\omega_0 \cdot L_{re}}{R_L} \tag{4.3}$$

During the reasoning to choose the coil radius, a parametric analysis aiming to evaluate the best ratio that would provide the widest tolerance of misalignment during the landing procedure of the drone on the charging base was conducted. This analysis was run considering both coils with a number of turns of 10. The results, derived from implementing the system on Comsol Multiphysics software, are shown in 4.2. A clear result is that a difference between the radii of 20 mm permits a large misalignment tolerance. Given this condition, the coupling coefficient, defined as $k = M/\sqrt{L_{tr}L_{re}}$, remains within a 5% variation from the value assumed under conditions of perfect alignment up to a displacement of 22 mm.

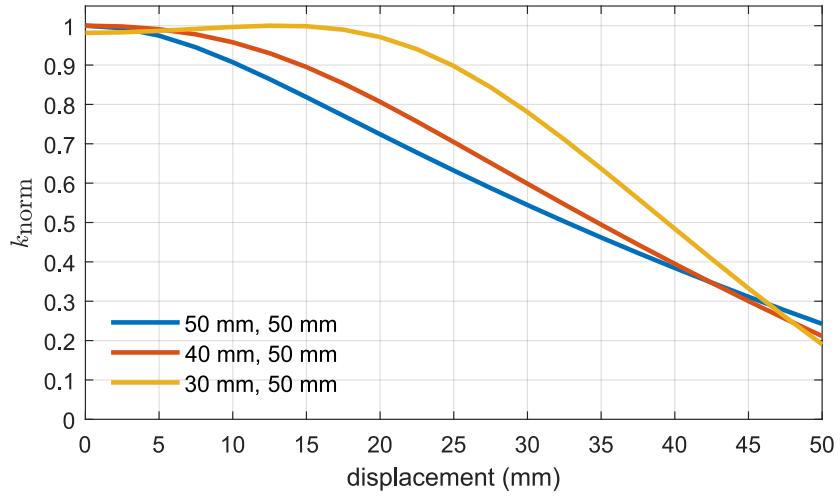

Figure 4.2: Graphical representation of the result of the simulation on Comsol. Coupling coefficient (normalized) as a function of the misalignment for different transmitter and receiver radii. Image retrieved from [38].

4.2 Coils' best design and mounting position

As reported in [38], three different designs in two possible mounting positions were tested and compared. As listed in Table 4.2, the constraints on radii developed in the previous section are respected. In addition, a ferrite disk is taken into analysis.

Table 4.2: Coils designs and mounting positions tested in [38].

Design	**Mounting position**
Tr50-Re30 without ferrite	center
Tr50-Re30 without ferrite	edge
Tr50-Re30 with ferrite	center
Tr50-Re30 with ferrite	edge
Tr30-Re50 with ferrite	center
Tr30-Re50 with ferrite	edge

The study [38] concludes that all three systems are capable of processing power within the range of 129-132 W, providing a safe operational margin that ensures quasi-N+1 redundancy. Among the evaluated configurations, the Tr30-Re50 configuration implementing ferrite disks consistently demonstrates superior performance across all scenarios. However, this design's main drawback is its significant weight, which is nearly five times greater than that of the ferrite-free counterpart. Regarding module position, the most favorable mounting location is at the extremities of the landing gear. This positioning minimizes the induction of eddy currents in the drone chassis, which would otherwise lead to increased energy losses. In Table 4.3, the parameters of the chosen design are reported.

Table 4.3: Main parameters of the Tr30-Re50 with ferrite design.

Parameter	Symbol	Value
Transmitter coil radius	$r_{\mathrm{tr,coil}}$	30 mm
Transmitter coil layers	-	2
Transmitter coil turns	N_{tr}	32 (2·16)
Transmitter coil self-inductance	L_{tr}	58.5 µH
Transmitter coil resistance	R_{tr}	95 mΩ
Ferrite plate thickness	Fe tk	2 mm
Ferrite plate radius	$r_{\mathrm{re,fe}}$	50 mm
Receiver coil radius	$r_{\mathrm{re,coil}}$	48 mm
Receiver coil layers	-	1
Receiver coil turns	N_{re}	10
Receiver coil self-inductance	L_{re}	25.0 µH
Receiver coil resistance	R_{re}	58 mΩ
Receiver coil mass	w_{Cu}	24.2 g
Ferrite plate mass	w_{Fe}	75.3 g

4.3 Design of the coupler from scratch

Referring to the design of Section 4.2, the solutions to physically realize the system are to construct the coils from scratch or search for coils available on the market.

The result from the study described in Section 4.2 requires two coils with ferrite plates. The market research started with the objective of ferrite disks of a diameter of 60 mm and 100 mm. Unfortunately, the survey revealed only disks with a maximum diameter of 50 mm. As a result, a disk for the transmitter is available, but for the receiver, the goal changes to square shapes. The dimension of interest is the circumscribed square of the circumference, so 100x100 mm. Two solutions were found and presented: LAIRD MM1400-300 [41] (36 mm in diameter) for the transmitter and KEMET FPL100-100-4-BH1T [42] (100 mm x 100 mm x 4 mm) for the receiver.

The second task is to calculate the required length of litz wire. Due to the design result, the section's diameter of the required litz wire is 1 mm. The following solution is proposed by solving a simple geometric problem. Knowing all the geometric parameters about the coil, such as external radius, number of turns and section of the wire, the total length of wire is the summation of the circumference lengths by decreasing radius. A graphical representation of the reasoning is reported in Figure 4.3, and the calculation is performed via Equations 4.4 and 4.5.

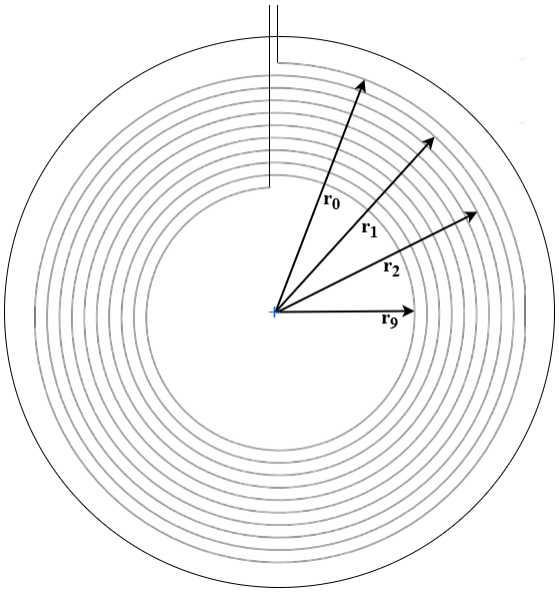

Figure 4.3: Graphical representation of the geometrical problem to resolve for obtaining the total lengths of the coils. In particular, here is represented the receiving coil's problem.

$$l_{re} = \sum_{i=0}^{N_{re}-1} 2 \cdot \pi \cdot (r_{\text{re,coil}} - i) = 2'733.19 \text{ mm} \simeq 2.8 \text{ m} \tag{4.4}$$

Same equation for transmitting coil, but taking into account that 2 layers are required.

$$l_{tr} = \sum_{i=0}^{N_{tr}-1} 2 \cdot \pi \cdot (r_{\text{tr,coil}} - i) \cdot 2 = 4'523.9 \text{ mm} \simeq 4.6 \text{ m} \tag{4.5}$$

$$l_{re} + l_{tr} \simeq 7.4 \text{ m} \tag{4.6}$$

To build both receiver and transmitter coils with the same type of wire, the minimum length needed is 7.4 m. After a market review, the two listed litz wires can be employed. The BLOCK CUL 500/1.0 [43] with 1 mm diameter, a current rating of 2.8 A and maximum current density of 3.6 A/mm^2 or the BQ DN2E 100 [44] with 1 mm diameter, a current rating of 2.3 A and maximum current density of 2.87 A/mm^2. The realization of the coils from scratch has the advantage of perfectly respecting the design; However, it is onerous. Better to look for coils already made, as will be presented in the next subsection.

4.4 Coils' market review

Given the requirements listed in Table 4.3, various commercially available coils have been analyzed. A Market review taking into account the major electronic brands (**Würth Elektronik**[45], **TDK**[46], **Signal Bel**[47], **Vishay**[48]) is presented in the following. In Table 4.4 are reported for each considered coil: brand, code, ferrite diameter and radius, wire section diameter, number of turns, auto inductance, DC resistance, input voltage, rated current, and power capability. A key aspect in choosing the coils is the radius ratio between the transmitter and receiver radii. For this reason, two variables are calculated for each coil. Given the ratio between the ideal coils:

$$TrRe_{\text{idealRatio}} = \frac{r_{\text{tr,coil}}}{r_{\text{re,coil}}} = \frac{30\text{ mm}}{50\text{ mm}} = 0.6 \tag{4.7}$$

- If the analyzed coil is taken as the receiver, then the ideal transmitter radius would be:

$$Tr_{\text{idealRadius}} = r_{\text{analyzedCoil}} \cdot TrRe_{\text{idealRatio}} \tag{4.8}$$

- If the analyzed coil is taken as the transmitter, then the ideal receiver radius would be:

$$Re_{\text{idealRadius}} = \frac{r_{\text{analyzedCoil}}}{TrRe_{\text{idealRatio}}} \tag{4.9}$$

Table 4.4: Review of the IPT coil market.

Brand	Code	Ferrite diameter [mm]	Ferrite radius [mm]	Coil diameter [mm]	Wire diameter [mm]	N. turns	N. layers	Inductance [μH]	R DC [mΩ]	V Input [V]	I Rated [A]	Q-factor	Power capability [W]	If Tr ideal Re radius [mm]	If Re ideal Tr radius [mm]
Würth Elektronik	760308101219	15.00	7.50	10.00	1.20	30	1	11.80	750.0	20.00	0.70	13	5	12.50	4.50
Würth Elektronik	760308101220	17.00	8.50	12.20	1.20	36	2	12.60	340.0	20.00	1.10	20	20	14.17	5.10
TDK	WT202012-15F2-1D	20.30	10.15	18.00		20	2	6.20	95.0					16.92	6.09
Würth Elektronik	760308101106	20.50	10.25	16.50	1.20	8	2	2.50	90.0	20.00	2.50	30		17.08	6.15
Würth Elektronik	760308101105	20.50	10.25	10.90	1.20	10	2	3.30	90.0		3.00	30		17.08	6.15
Würth Elektronik	760308101104	20.50	10.25	15.70	1.20	14	2	6.80	125.0	20.00	2.50	42		17.08	6.15
Signal Bel	WRSC-47R0K-08	26.00	13.00					47.00	500.0		1.50	25		21.67	7.80
Würth Elektronik	760308101309	26.30	13.15	24.48	1.20	14	1	10.00	350.0	20.00	1.50	20	20	21.92	7.89
Würth Elektronik	760308101303	26.30	13.15				3	47.00	500.0		1.50	25	20	21.92	7.89
TDK	WR28284O-37K2-LR3	28.00	14.00	26.00		37	1	46.00	1250.0					23.33	8.40
Würth Elektronik	760308101103	30.00	15.00	28.00	2.00	20	2	6.50	200.0		3.00	35		25.00	9.00
Würth Elektronik	760308101107	31.00	15.50	29.00	1.20	20	2	24.00	315.0	20.00	2.00	55		25.83	9.30
Vishay	IWTX47R0DAEB6R3JF1	47.00	23.50	44.00	1.20	10	1	6.30	40.0		7.00			39.17	14.10
Vishay	IWTX47R0EBEB240JF1	47.00	23.50	44.00		20	2	24.00	75.0		6.00	200		39.17	14.10
Würth Elektronik	760308101304	47.50	23.75	43.50	2.00	9	1	6.30	48.0		8.00	115		39.58	14.25
Würth Elektronik	760308101302	50.00	25.00	44.00	2.00	8	1	5.30	35.0		8.00	100		41.67	15.00
Würth Elektronik	760308100143	50.00	25.00	38.00	2.00	10	2	6.00	18.0		12.00	180		41.67	15.00
Vishay	IWTX50R0DZEB6R3KF1	50.00	25.00	44.00	1.20	20	2	6.30	25.0		10.00	90		41.67	15.00
TDK	WT505090-20K2-A10-G	50.00	25.00	43.00		20	2	24.00	100.0	19.00				41.67	15.00
Vishay	IWTX50R0CZEB6R3KF1	50.00	25.00	44.00	1.20	10	1	6.30	45.0		5.00	120		41.67	15.00
Würth Elektronik	760308101411	50.00	25.00	42.00	2.00	10	1	6.30	48.0	20.00	7.50		150	41.67	15.00
Würth Elektronik	760308100111	50.00	25.00	46.00	2.00	10	1	6.30	48.0		6.00	120		41.67	15.00
Würth Elektronik	760308100141	50.00	25.00	43.00	2.00	14	2	10.00	30.0		9.00	180		41.67	15.00
Würth Elektronik	760308101141	50.00	25.00	38.00	2.00	14	2	10.00	30.0	20.00	9.00	220	150	41.67	15.00
Würth Elektronik	760308100110	50.00	25.00	43.00		20	2	24.00	100.0		6.00	180		41.67	15.00
Würth Elektronik	760308101410	50.00	25.00	42.00	2.00	20	2	24.00	100.0	20.00	5.50	170	100	41.67	15.00
Vishay	IWTX55R0DZEB8R9KF1	55.00	27.50	51.00	1.20	10	1	8.90	55.0		6.00	99	15	45.83	16.50
	Ideal Transmitter	60.00	30.00	30.00	1.00	32	2	58.50	95.0	24.00	2.14		33	50.00	18.00
Würth Elektronik	760308101311	70.00	35.00	64.00	3.00	11	1	5.80	14.0	20.00	21.00	220	400	58.33	21.00
Würth Elektronik	760308101310	75.00	37.50					24.00	110.0		7.50	155	100	62.50	22.50
	Ideal Receiver	100.00	50.00	48.00	1.00	10	1	25.00	58.0					83.33	30.00

4.4.1 Testing the performance of market coils

The process of choosing the coils is not based only on geometrical aspects but also on magnetic performance. Based on data collected in Table 4.4, the most suitable coils are divided into 9 couples reported in Table 4.6. A MATLAB script that interfaces with FEMM makes it possible to magnetically test the couples of coils. This script takes as input the geometrical characteristics of the coils and the gap, draws the scheme 4.4 on FEMM, imposes the materials properties of Table 4.5, launches the FEMM simulation, and retrieves the results. The objective of the test is to calculate the maximum gap between the coils to reach the target mutual inductance, in addition, the coupling coefficient is calculated (by Equation A.9). To reduce the computational effort, the implementation uses cylindrical coordinates and analyzes only half system, as shown in Figure 4.4. In Figure 4.5 the implementation on FEMM is shown.

The magnetic problem is solved by imposing the Neumann boundary condition [49]. When modeling open boundaries (e.g. air domains around a magnetic device), the assumption is that the normal derivative of the potential is zero. This assumption approximates a boundary far from the magnetic source.

The materials used in the simulations are listed in Table 4.5. In particular, magnetic relative permeability along the azimuth coordinate (μ_r), magnetic relative permeability along the axial coordinate (μ_Z) and electrical conductivity (σ [MS/m]).

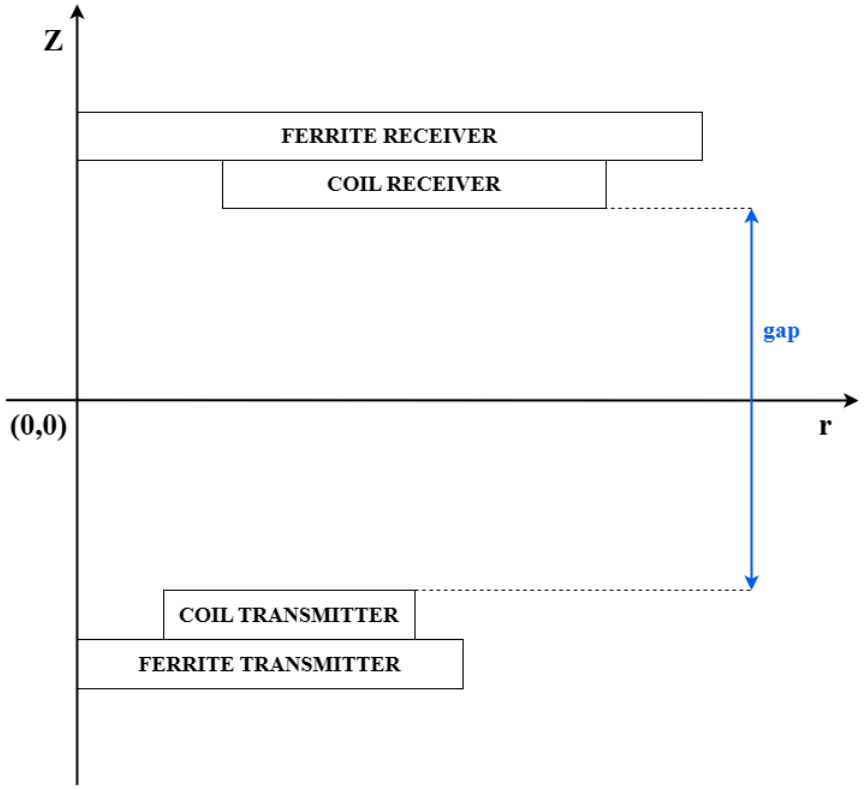

Figure 4.4: Cylindrical coordinates used for the implementation on FEMM.

Table 4.5: Properties of the materials used in the FEMM simulations.

Material	B-H Curve	μ_r	μ_Z	σ [MS/m]
Air	Linear relationship	1	1	0
Copper	Linear relationship	1	1	58
Ferrite	Linear relationship	2150	2150	0

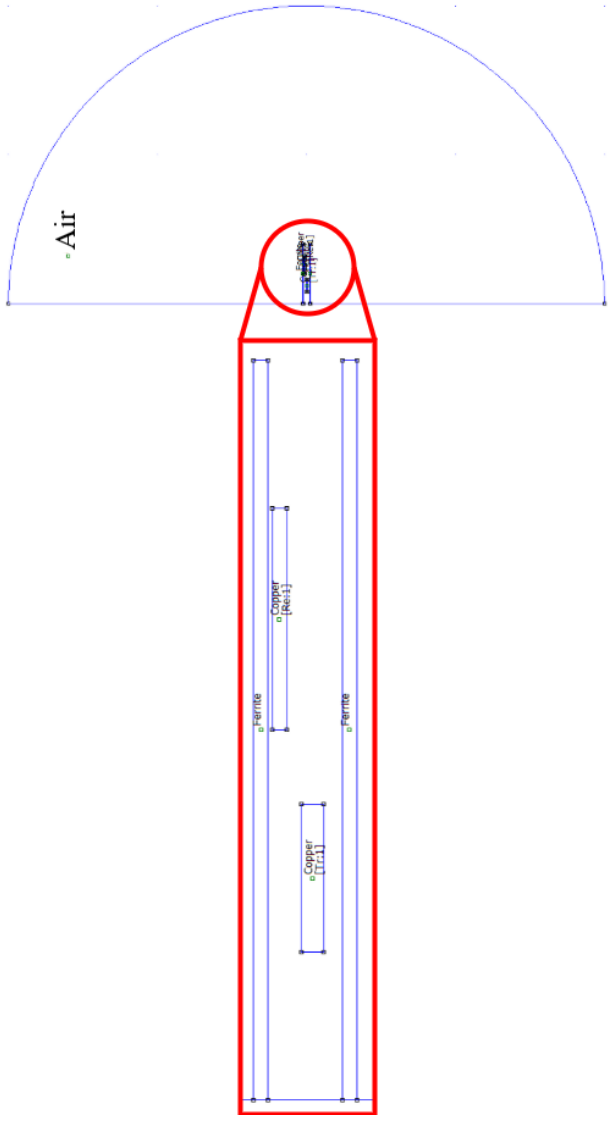

Figure 4.5: Graphical model of the FEMM implementation.

4.4.2 Market coils' performance outcome

For each couple of coils listed in Table 4.6, the test described in Subsection 4.4.1 is performed. The results are collected in Table 4.6 as well.

Table 4.6: Outcomes of FEMM simulations.

Simulation code	Brand	Code	Ferrite diameter [mm]	Ferrite radius [mm]	Coil diameter [mm]	Wire diameter [mm]	N. turns	N. layers	Inductance [μH]	R DC [mΩ]	V Input [V]	I Rated [A]	Q-factor	Power capability [W]	Ratio Tr/Re	Gap [mm]	M [μH]	k
SC1	Vishay	IWTX47R0EBEB240JF1	47	23.50	44.00		20.00	2	24	75.00		6.00	200.00		0.60	14.00	11.32	0.34
	TDK	WR282840-37K2-LR3	28	14.00	26.00		37.00	1	46	1250.00								
SC2	Würth Elektronik	760308100110	50	25.00	43.00		20.00	2	24	100.00		6.00	180.00		0.56	12.00	11.41	0.34
	TDK	WR282840-37K2-LR3	28	14.00	26.00		37.00	1	46	1250.00								
SC3	TDK	WT505090-20K2-A10-G	50	25.00	43.00		20.00	2	24	100.00	19.00				0.56	13.00	11.48	0.34
	TDK	WR282840-37K2-LR3	28	14.00	26.00		37.00	1	46	1250.00								
SC4	Würth Elektronik	760308101410	50	25.00	42.00	2.00	20.00	2	24	100.00	20.00	5.50	170.00	100	0.62	9.00	11.36	0.53
	Würth Elektronik	760308101107	31	15.50	29.00	1.20	20.00	2	24	315.00	20.00	2.00	55.00					
SC5	Würth Elektronik	760308101410	50	25.00	42.00	2.00	20.00	2	24	100.00	20.00	5.50	170.00	100	0.56	12.00	10.93	0.33
	TDK	WR282840-37K2-LR3	28	14.00	26.00		37.00	1	46	1250.00								
SC6	Würth Elektronik	760308101304	48	23.75	43.50	2.00	9.00	1	6	48.00		8.00	115.00		0.55	4.00	11.40	0.66
	Würth Elektronik	760308101303	26	13.15			48.00	3	47	500.00		1.50	25.00	20				
SC7	Vishay	IWTX47R0EBEB240JF1	47	23.50	44.00		20.00	2	24	75.00		6.00	200.00		0.56	12.00	11.41	0.36
	Würth Elektronik	760308101303	26	13.15			48.00	3	47	500.00		1.50	25.00	20				
SC8	Würth Elektronik	760308101310	75	37.50			16.00		24	110.00		7.50	155.00	100	0.67	18.00	11.43	0.50
	Würth Elektronik	760308101410	50	25.00	42.00	2.00	20.00	2	24	100.00	20.00	5.50	170.00	100				
SC9	Würth Elektronik	760308101310	75	37.50			16.00		24	110.00		7.50	155.00	100	0.63	19.00	11.45	0.47
	Vishay	IWTX47R0EBEB240JF1	47	23.50	44.00		20.00	2	24	75.00		6.00	200.00					

The most interesting couple of coils are the one tested in simulation with code 8. They are Würth Elektronik 760308101310 as receiver and Würth Elektronik 7603081014 10 as transmitter (the characteristics are reported in Subsection 4.4.3). This couple presents a very good Tr/Re radius ratio (compared to the ideal 4.7) and achieves the target mutual inductance with the highest gap (18 mm) and coupling coefficient (0.5). The magnetic flux density distribution of SC8 is reported in Figure 4.6.

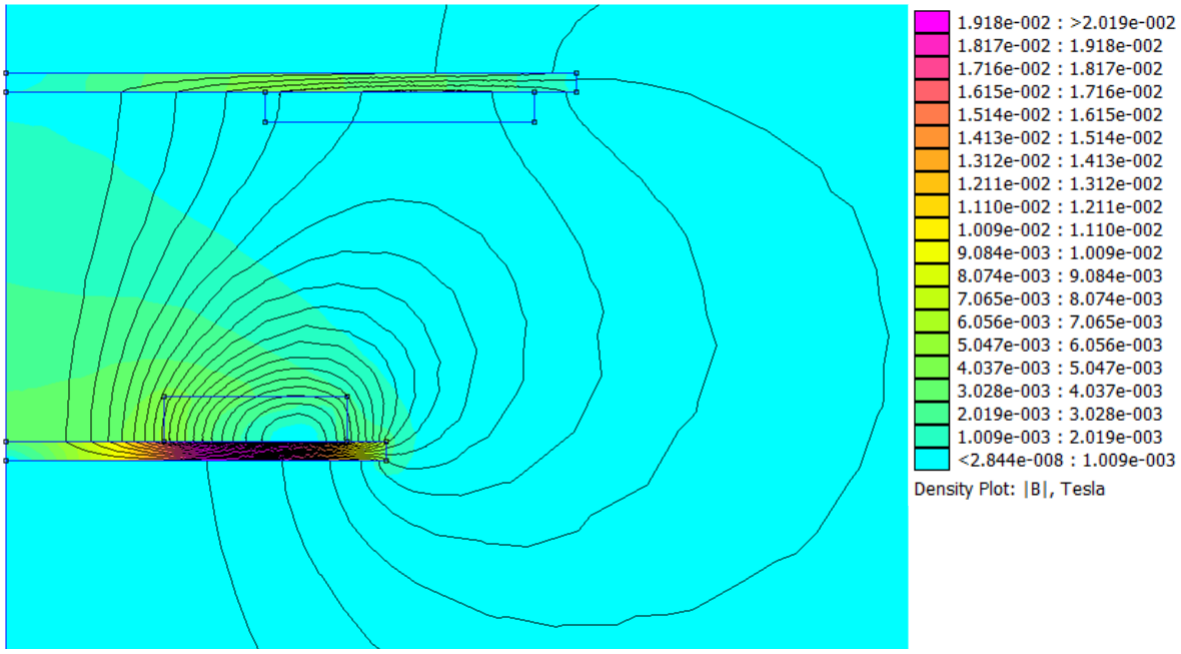

Figure 4.6: Graphical outcome of the magnetic flux density distribution of SC8 from FEMM simulation.

4.4.3 Würth Elektronik coils' characteristics

The listed values in Table 4.7 are the parameters of the coils couple composed of Würth Elektronik 760308101310 as receiver and Würth Elektronik 760308101410 as transmitter. This couple will be used in the following analysis. Both coils are Qi-compliant and present the same value of self-inductance. A photo of the coils is reported in Figure 4.7.

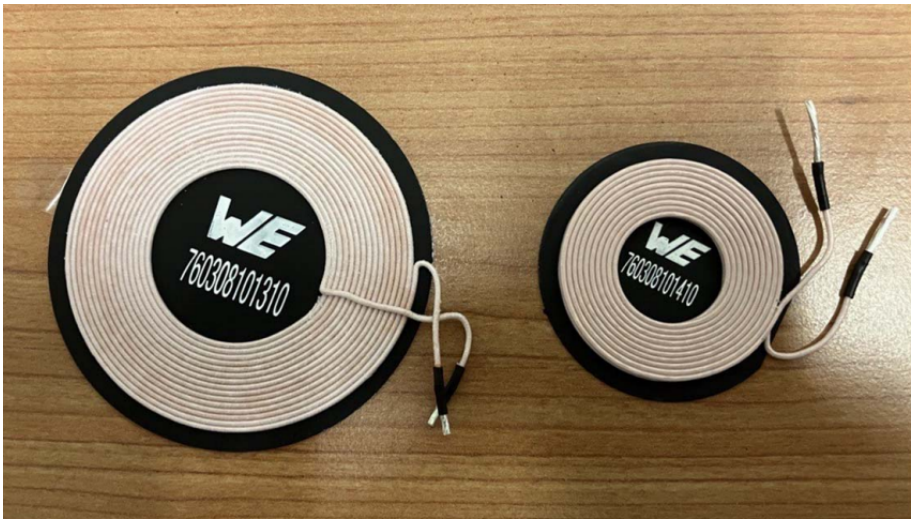

Figure 4.7: Photo of the receiver (on the left) and the transmitter (on the right) coils. Image retrieved from [50].

Table 4.7: Characteristics of the chosen Würth Elektronik coils couple.

Parameter	**Symbol**	**Value**
Transmitter coil radius	$r_{tr,coil}$	25 mm
Transmitter coil layers	-	2
Transmitter coil turns	N_{tr}	20 $(2 \cdot 10)$
Transmitter coil self-inductance	L_{tr}	24 µH
Transmitter coil resistance	R_{tr}	100 mΩ
Ferrite plate radius	$r_{re,fe}$	25 mm
Receiver coil radius	$r_{re,coil}$	37.5 mm
Receiver coil layers	-	1
Receiver coil turns	N_{re}	16
Receiver coil self-inductance	L_{re}	24.0 µH
Receiver coil resistance	R_{re}	110 mΩ

Chapter 5

Module Model

Following the work done in Chapter 4, a modular system is proposed. The singular module is an IPT resonant series-series compensated system.

5.1 Model's description

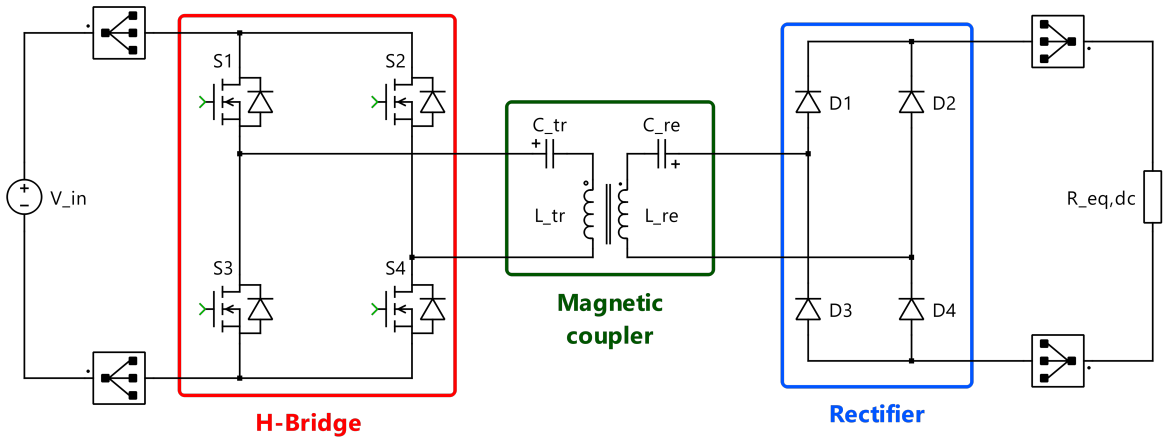

Figure 5.1: Circuit diagram of the chosen model.

The proposed singular module model is composed of an inverter (H-Bridge) realized with 4 MOSFETs powered by a DC source (V_{in}). The inverter powers the induction coupler realized by the transmitting (L_{tr}) and receiving (L_{re}) coils. As a series-series compensated system, to achieve the resonance condition, 2 capacitances are inserted in series to the transmitting (L_{tr}) and receiving (L_{re}) coils, respectively C_{tr} and C_{re}. Then a full-wave diode rectifier, consisting of 4 diodes, is inserted to power the load. The load is modeled as a resistance $R_{eq,dc}$. To fully analyze the module's displacement impact, no filtering capacitance is installed. Next, as shown in Figure 5.1, all the modules are connected in parallel.

5.2 Parameters of the single module

The parameters of the model are divided into imposed parameters (from the previous analysis) collected in Table 5.1 and calculated parameters gathered in Table 5.2.

Table 5.1: Single module imposed parameters.

Parameter	**Symbol**	**Value**
Working frequency or resonant frequency	f	205 kHz
DC input voltage	V_{in}	24 V
Output voltage	V_{out}	24 V
Rated output power (single module)	P_{SMO}	33 W
Transmitting inductance	L_{tr}	48 µH
Receiving inductance	L_{re}	24 µH

The calculations of the following parameters is performed as expressed in formulas listed in Appendix A.

Table 5.2: Single module calculated parameters.

Parameter	**Symbol**	**Value**
DC load resistance	$R_{eq,dc}$	17.5 Ω
AC load resistance	$R_{eq,ac}$	14.19 Ω
Transmitting compensation capacitance	C_{tr}	12.6 nF
Receiving compensation capacitance	C_{re}	25.1 nF
Mutual inductance	M	10.98 µH
Total output impedance (modulus)	Z_T	14.15 Ω
Coupling factor	k	0.32
Transmitting quality factor	Q_{tr}	4.37
Receiving quality factor	Q_{re}	2.18

5.2.1 Focus on the transmitting inductance

The goal of the resonance is to work in a low-resistance and non-reactive system. The designed L_{tr} is 24 µH, but a system like that (Table 5.3) presents the so-called *bifurcation phenomenon* (defined in [51]) in the behavior of the $\overline{Z_T}$ in frequency as shown in Figure 5.2. This behavior is a problem for the controllability of the system: if bifurcation phenomenon is present, the null phase point is an unstable point. Around the resonance, a slight change of the working frequency leads to the equivalent behavior of the system changing abruptly from inductive to capacitive or vice versa.

Switching a capacitive load involves managing the inrush current that occurs when a capacitor is charged or discharged. When a capacitive load is switched on, a high inrush current flows as the capacitor charges. This current can be significantly larger than the steady-state current and potentially damage the switching device.

Table 5.3: Model's parameters with bifurcation phenomenon (reporting only the different ones from Tables 5.1) and 5.2).

Parameter	**Symbol**	**Value**
Transmitting inductance	L_{tr}	24 µH
Receiving inductance	L_{re}	24 µH
Mutual inductance	M	10.98 µH
Transmitting compensation capacitance	C_{tr}	25.1 nF
Receiving compensation capacitance	C_{re}	25.1 nF
Total output impedance	Z_T	14.15 Ω
Coupling factor	k	0.46
Transmitting quality factor	Q_{tr}	2.19
Receiving quality factor	Q_{re}	2.18
Left frequency	f_{01}	169.8 kHz
Right frequency	f_{02}	278.4 kHz

Where the angular frequencies are calculated:

$$\omega_{01,02} = \omega_0 \frac{1}{\sqrt{1 \pm k\sqrt{1 - \frac{1}{2k^2}\left(\frac{1}{Q_{tr}^2} + \frac{1}{Q_{re}^2}\right)}}} \tag{5.1}$$

$$f_{01,02} = \frac{\omega_{01,02}}{2\pi} \tag{5.2}$$

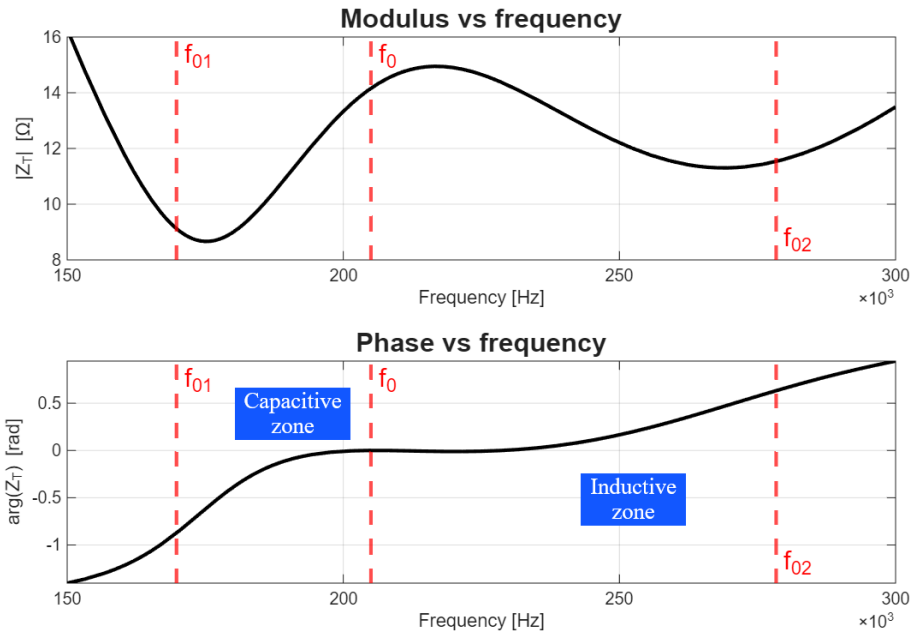

Figure 5.2: Plot of the modulus and argument of the total output impedance as the frequency varies. The bifurcation phenomenon is present.

For this reason, the L_{tr} is doubled up to 48 µH. Physically, two coils are connected in series, but only one of the two will couple with the receiver. This technique avoids the bifurcation phenomenon, leading to a behavior of the system in frequency as shown in Figure 5.3.

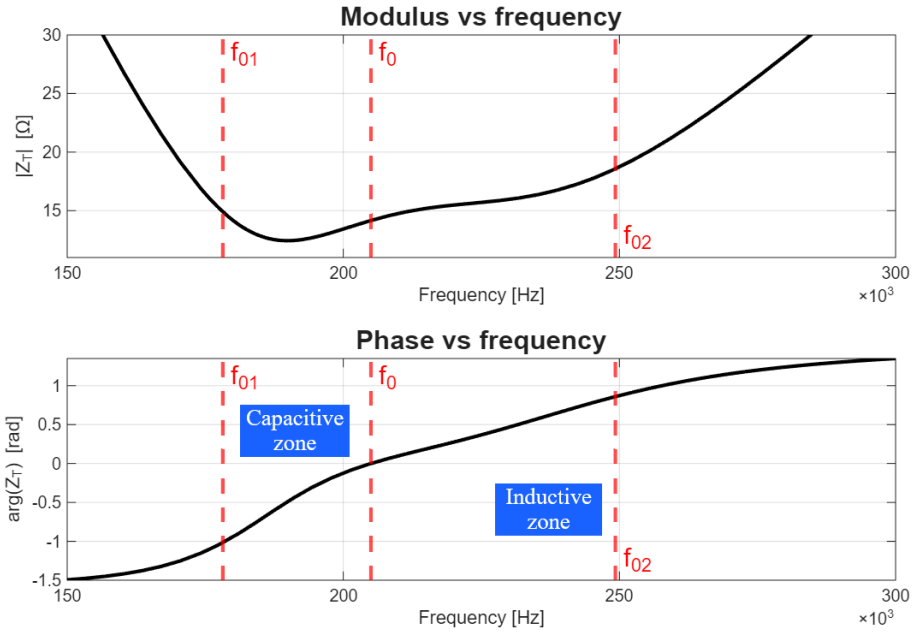

Figure 5.3: Plot of the modulus and argument of the total output impedance as the frequency varies. The bifurcation phenomenon is not present.

5.3 Parameters of the system with more than one module

As the number of modules ($N_{modules}$) becomes higher than one, the total output power ($P_{out,total}$) increases. So the representation of the load has to change. In Table 5.4, the values up to 4 modules, the maximum chosen number for this work, are reported.

$$P_{out,total} = P_{SMO} \cdot N_{modules} \tag{5.3}$$

$$R_{eq,dc} = \frac{V_{out}^2}{P_{out,total}} \tag{5.4}$$

$$R_{eq,ac} = \frac{8}{\pi^2} R_{eq,dc} \tag{5.5}$$

Table 5.4: More than one module calculated parameters.

$N_{modules}$	$P_{out,total}$	$R_{eq,dc}$	$R_{eq,ac}$
2	66 W	8.73 Ω	7.08 Ω
3	99 W	5.82 Ω	4.72 Ω
4	132 W	4.36 Ω	3.53 Ω

Chapter 6

Analysis Environment

To fully understand the behavior of the system, an interconnected and cooperative environment made up of Plexim PLECS, MathWorks MATLAB and Microsoft Excel was designed. As will be explained in Sections 6.1 and 6.2, the PLECS implementation will take as input the characterizing (and imposed) parameters of the specific simulation to perform, calculating the remaining parameters, and exporting the results as MATLAB MAT-files. Thereafter, MATLAB is employed to organize, analyze and build reports consisting of graphs and Microsoft Excel tables. As last resort, Microsoft Excel is used to access the reports and as a fast check for consistency of results.

6.1 Implementation on PLECS

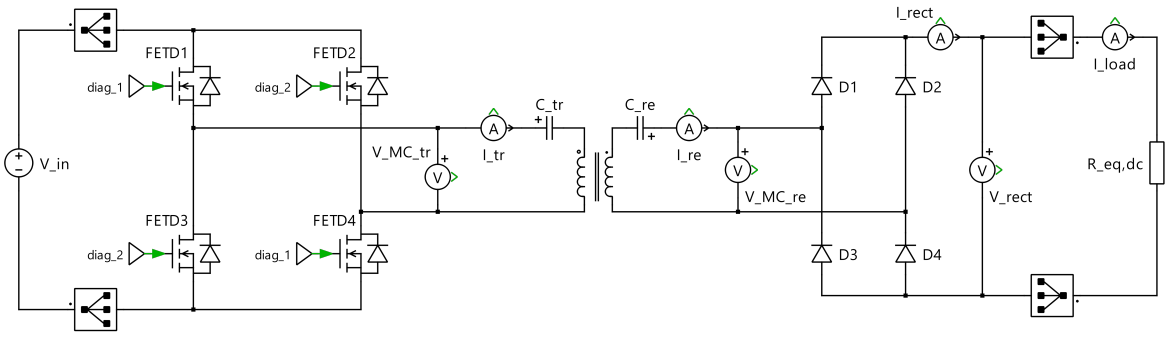

Figure 6.1: PLECS schematic of the system under analysis.

PLECS (Piecewise Linear Electrical Circuit Simulation) is a software tool developed by Plexim that provides system-level simulations of electrical circuits. It is specially designed for power electronics but can be used for any electrical network. PLECS includes the possibility of modeling controls and different physical domains (thermal, magnetic and mechanical) besides the electrical system.

The study continued by implementing the chosen model on PLECS as shown in Figure 6.1. The developed implementation features:

- takes in input the imposed parameters in Table 5.1;
- takes in input the number of modules $N_{modules}$;
- the number of simulations $N_{simulations}$ to perform. This feature will be exploited in Section 7.3 and Chapter 8;
- the possibility to fix the firing signal of each module:
  - No Displacement (ND) in Subsection 7.2.1;
  - Equal Displacement (ED) in Subsection 7.2.2;
  - Half Period Equal Displacement (HPED) in Subsection 7.2.3;
  - A given array of FSs to recreate the simulation condition of a configuration of interest.
- the possibility to randomly calculate the firing signals of the modules. This feature will be exploited in Section 7.3;
- the possibility to randomly vary the compensation capacitances. This feature will be exploited in Chapter 8.

Then the software fully automatically and parametrically calculates the values in Tables 5.2 and 5.4. Additionally, the PLECS implementation calculates and exports:

- Voltage ripple, V_{ripple} (Equation 6.2);

$$V_{load,delta} = V_{load,max} - V_{load,min} \tag{6.1}$$

$$V_{load,ripple} = \frac{V_{load,delta}}{V_{load,dc}} \tag{6.2}$$

- Voltage across the load, current and power on the load, DC and RMS values;
- Single module output DC power value (SMOP DC).

6.2 Auxiliary tools on MATLAB

The objective of PLECS is to perform the electric circuit simulation given the input parameters. Afterwards, MATLAB scripts are employed to organize, analyze and compile reports consisting of graphs and Excel datasheets. The developed programs are:

- Single simulation report. This program is developed to deeply analyze a single simulation. Given the simulation's code, the script gives as output an Excel table containing all the exported values from PLECS and a graphical report (Figure 6.2) with the percentage of displacement of FSs, the plot of the FSs and the shapes of voltage across the load and current on the load.

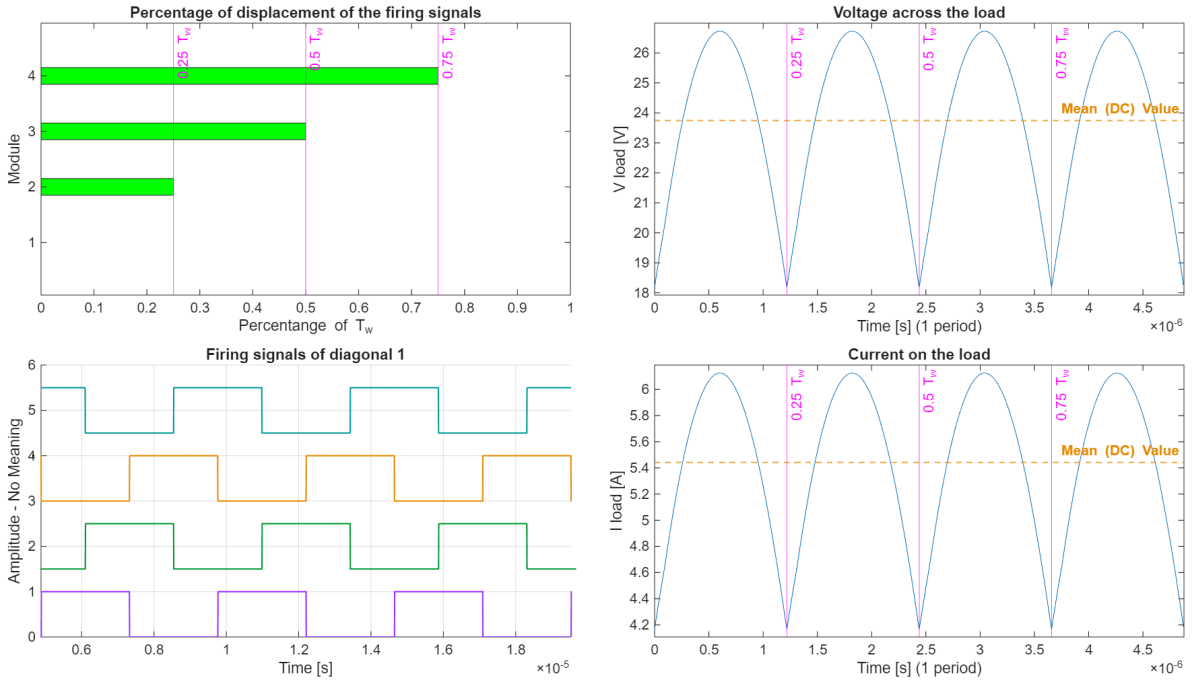

Figure 6.2: Single simulation report graphical output example. In particular: percentage of displacement of FSs (top-left), plot of the FSs (bottom-left), shapes of voltage across the load (top-right), and current on the load (bottom-right).

- Random displacement batch simulation report. As reported in Section 7.3, a study on the impact of a non-imposed control strategy of the modules' firing is done.
- Power DC versus ripple report. The two most important variables in this study are output power and voltage across the load ripple. In particular, the relationship between the two, covered in Subsection 7.3.1.
- Compensation capacitances uncertainty impact batch simulation report. Another performed study is on the impact of tolerances on the resonance capacitances on the system behavior in Chapter 8.

Chapter 7

Impact of the Displacement Between the Modules

7.1 Single module

The first step to go deep into the study of the interaction between the modules is to analyze the single one. In Figure 7.1 and Tables 7.1, 7.2, and 7.3, the results of this first simulation are reported. As shown in Figure 7.1 and reported in Table 7.3, the voltage across the load approximately follows the shape of what would be expected from the action of an FWR. The voltage oscillates from $\simeq 0$ V to $\simeq 36.4$ V, resulting in a ripple of $\simeq 152\%$. The voltage DC value across the load is $\simeq 24$ V, as requested from the previous analysis. The output DC power is $\simeq 40$ W, higher than the target power of 33 W. As the implemented system presents no dissipation (make an exception for the resistance of the coils), over-sizing the system is a good practice for achieving the target output power despite the losses of a real-world implementation.

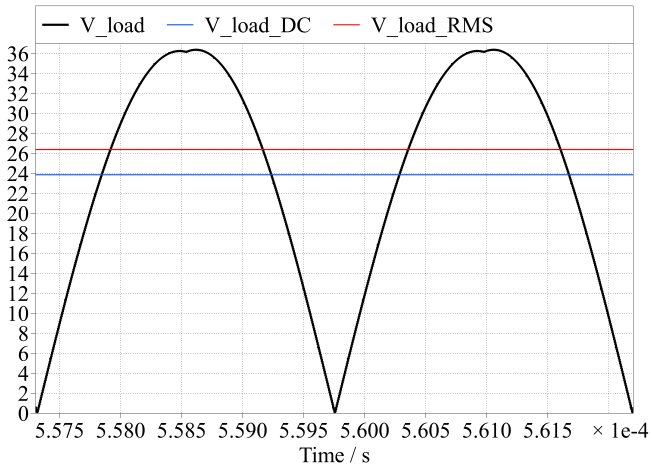

Figure 7.1: Instant voltage across the load in the case of a singular module. The voltage DC and RMS values are reported as well.

Table 7.1: Single module DC values.

$N_{modules}$	$V_{load,dc}$	$I_{load,dc}$	$P_{load,dc}$
1	23.880 V	1.3681 A	39.948 W

Table 7.2: Single module RMS values.

$N_{modules}$	$V_{load,rms}$	$I_{load,rms}$	$P_{load,rms}$
1	26.406 V	1.5129 A	48.422 W

Table 7.3: Single module ripple values.

$N_{modules}$	$V_{load,dc}$	$V_{load,max}$	$V_{load,min}$	$V_{load,delta}$	Ripple
1	23.880 V	36.3912 V	0.110573 V	36.2806 V	1.5193

7.2 FD - Fixed Displacement

As will be explained in this section, the impact on the behavior of the whole system of the displacement between the modules is huge. The H-bridges of the modules work exactly the same. The first diagonal is fired at a given instant, then the second diagonal is fired after half period, resulting in a duty cycle (D, Equation 7.1) of 0.5. In the following tables, the FSs of the first diagonals will be reported as an array.

$$D = \frac{T_{on}}{T} = \frac{2.439\ \mu s}{4.878\ \mu s} = 0.5 \tag{7.1}$$

7.2.1 ND - No Displacement

The first case involves ensuring that all modules work simultaneously. This results in no interaction between the modules, so all of them are working as identical systems in parallel. It is possible to highlight:

1. The total output current is the sum of the singular module output current. Currents $I_{load,dc}$ and $I_{load,rms}$ in Table 7.4 are equal to $I_{load,dc}$ and $I_{load,rms}$in Table 7.1 times $N_{modules}$;

2. As shown in Figure 7.2 and reported in Table 7.6, $V_{load,dc}$, $V_{load,max}$ and $V_{load,min}$ do not change in increasing the number of modules. So the voltage ripple does not change with respect to the case of a singular module (Section 7.1);

3. Combination of points 1 and 2 results in the maximum output power for each number of modules.

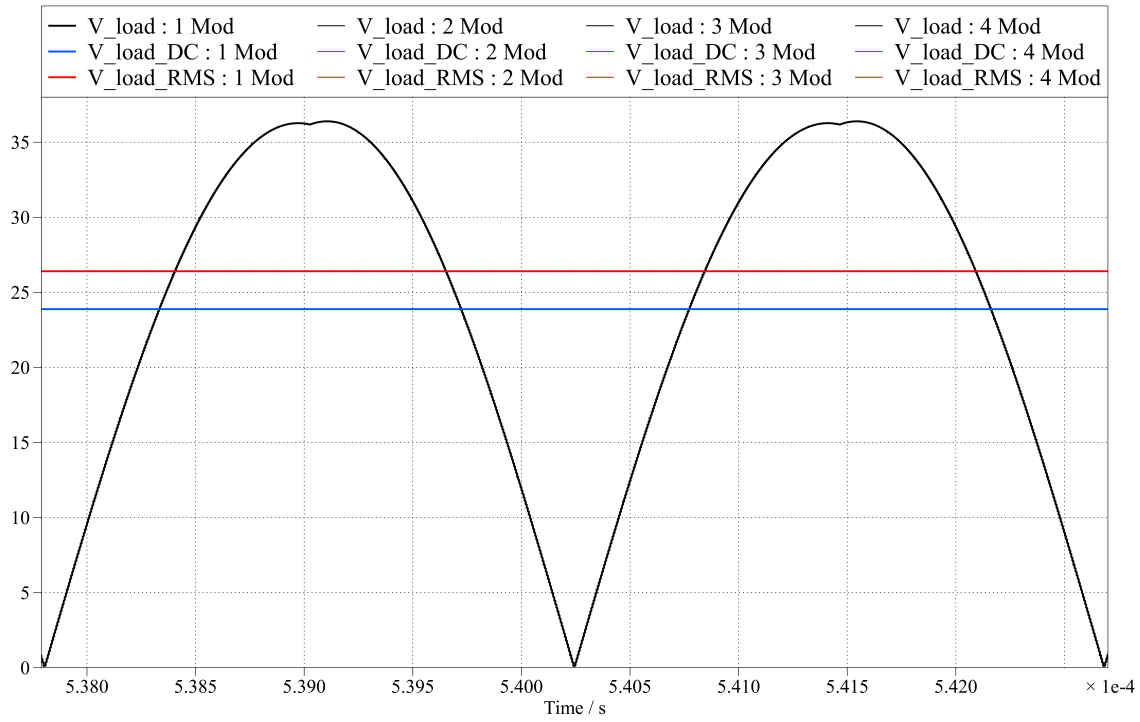

Figure 7.2: Instant voltage across the load in the case of no displacement (ND) with 1, 2, 3 and 4 modules. The DC and RMS voltage values are depicted as well.

Table 7.4: No displacement DC values.

$N_{modules}$	Firing signals	$V_{load,dc}$	$I_{load,dc}$	$P_{load,dc}$
2	[0 0]	23.881 V	2.7363 A	79.8972 W
3	[0 0 0]	23.881 V	4.1044 A	119.8459 W
4	[0 0 0 0]	23.881 V	5.4725 A	159.7927 W

Table 7.5: No displacement RMS values.

$N_{modules}$	$V_{load,rms}$	$I_{load,rms}$	$P_{load,rms}$
2	26.4062 V	3.0257 A	96.8453 W
3	26.4062 V	4.5386 A	145.2679 W
4	26.4062 V	6.0514 A	193.6883 W

Table 7.6: No displacement ripple values.

$N_{modules}$	$V_{load,dc}$	$V_{load,max}$	$V_{load,min}$	$V_{load,delta}$	Ripple
2	23.881 V	36.3914 V	0.11057 V	36.281 V	1.51924
3	23.881 V	36.3914 V	0.11057 V	36.281 V	1.51924
4	23.881 V	36.3914 V	0.11057 V	36.281 V	1.51924

7.2.2 ED - Equal Displacement

In this subsection, the control strategy consists of dividing the working period equally by the number of modules (Expression 7.2).

$$Mod_{displ} = \frac{T}{N_{modules}} \tag{7.2}$$

- In the case of 2 modules, this strategy has no effect, the two modules are displaced by half period, so they have no interaction. There is no difference with the case of ND in Subsection 7.2.1.
- In the case of 3 modules, the change is substantial. The voltage oscillation shrinks a lot around the voltage DC value, resulting in a huge improvement in voltage ripple, which is now $\simeq 14\%$. On the other hand there is an important reduction in output power, which now is $\simeq 97$ W, with a reduction of $\simeq 20\%$.
- Last configuration is the case of 4 modules, which experiences an improvement in ripple, that is now $\simeq 36\%$, with the side effect of a reduction in output power of $\simeq 19\%$. This first improvement is not the best achievable, because the system is working as 2 subsystems of 2 modules displaced by half period as shown in Figure 7.3. In fact, in the next subsection, better performance will be reached.

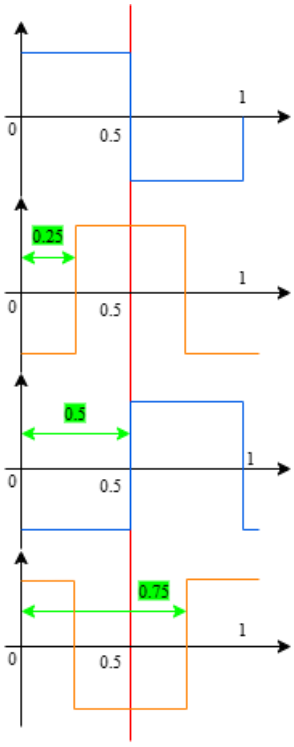

Figure 7.3: Graphical representation of the FSs for a system composed of 4 modules with fixed ED. It works as 2 subsystems (blue and orange) of 2 modules displaced by half period.

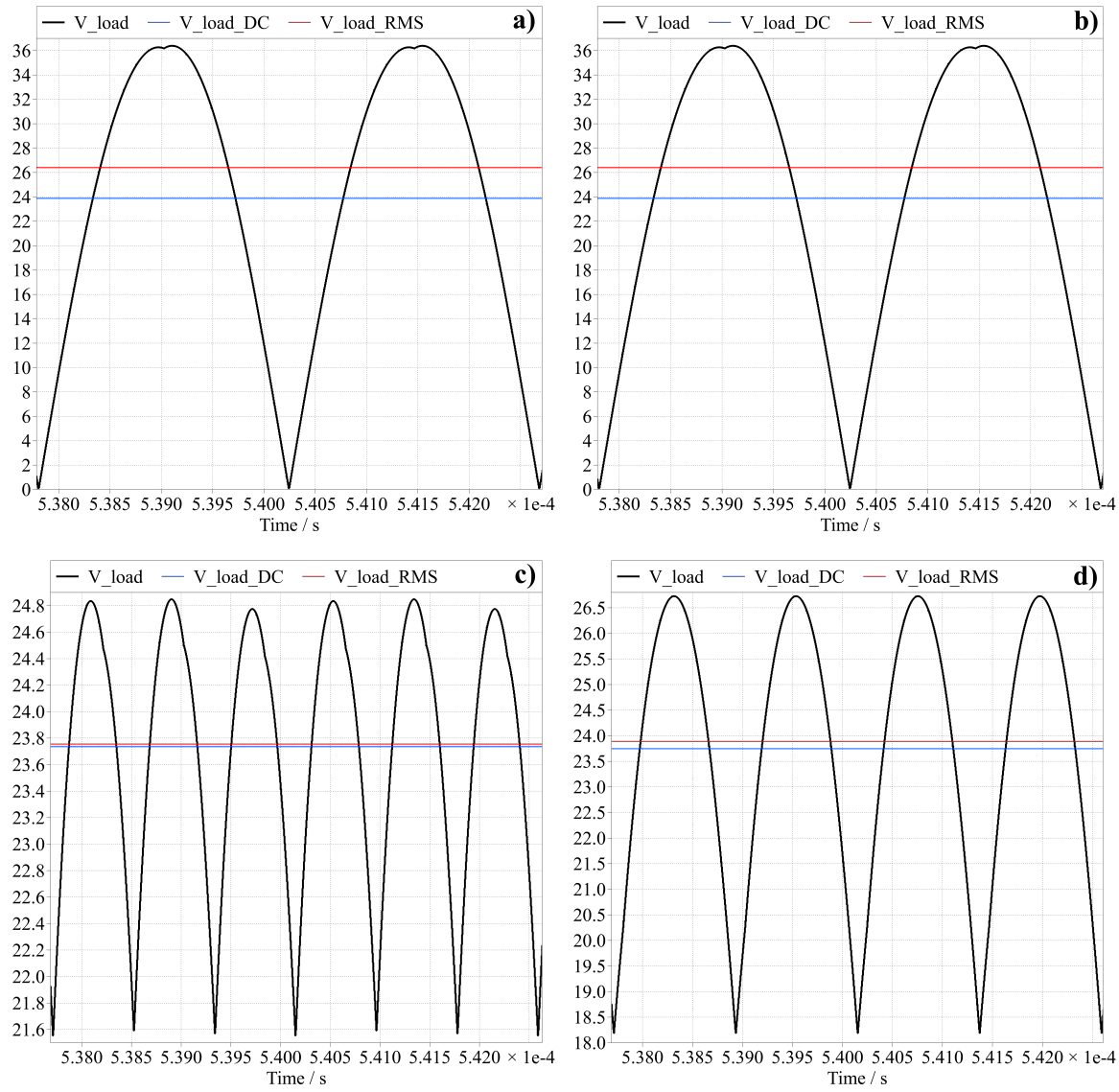

Figure 7.4: Instant voltage across the load in the case of equal displacement (ED) with 1 (a), 2 (b), 3 (c) and 4 (d) modules. The DC and RMS voltage values are depicted as well.

Table 7.7: Equal displacement DC values.

$N_{modules}$	Firing signals	$V_{load,dc}$	$I_{load,dc}$	$P_{load,dc}$
2	[0 0.5]	23.881 V	2.7363 A	79.8972 W
3	[0 0.33 0.66]	23.7357 V	4.0796 A	96.990 W
4	[0 0.25 0.5 0.75]	23.7466 V	5.4420 A	130.7881 W

Table 7.8: Equal displacement RMS values.

$N_{modules}$	$V_{load,rms}$	$I_{load,rms}$	$P_{load,rms}$
2	26.4062 V	3.0257 A	96.8453 W
3	23.7552 V	4.0829 A	97.2983 W
4	23.8895 V	5.4747 A	133.6544 W

Table 7.9: Equal displacement ripple values.

$N_{modules}$	$V_{load,dc}$	$V_{load,max}$	$V_{load,min}$	$V_{load,delta}$	Ripple
2	23.881 V	36.3914 V	0.110573 V	36.2808 V	1.51923
3	23.736 V	24.8481 V	21.555 V	3.2931 V	0.13874
4	23.7466 V	26.7269 V	18.1918 V	8.5351 V	0.35942

7.2.3 HPED - Half Period Equal Displacement

In this subsection, the control strategy consists of dividing half of the working period equally by the number of modules (Expression 7.3).

$$Mod_{displ} = \frac{T}{2 \cdot N_{modules}} \tag{7.3}$$

- In the case of 2 modules, the change is substantial. The voltage oscillation shrinks a lot around the voltage DC value, resulting in a huge improvement in voltage ripple, which is now $\simeq 36\%$ (the same value as 4 modules system with ED strategy). A side effect is an important reduction in output power, which now is $\simeq 65$ W, a reduction of $\simeq 13\%$ with respect to the ED (and as said ND) case.

- In the case of 3 modules, this strategy has no effect. There is no difference with the case of ED in Subsection 7.2.2.

- Instead, the case of 4 modules experiences the best improvement in ripple. The voltage oscillation is $\simeq 3.3$ V around the DC value, resulting in a ripple of $\simeq 8\%$. Unfortunately, the output power drops a lot from $\simeq 160$ W of the ND case to $\simeq 129$ W, with a reduction of $\simeq 20\%$.

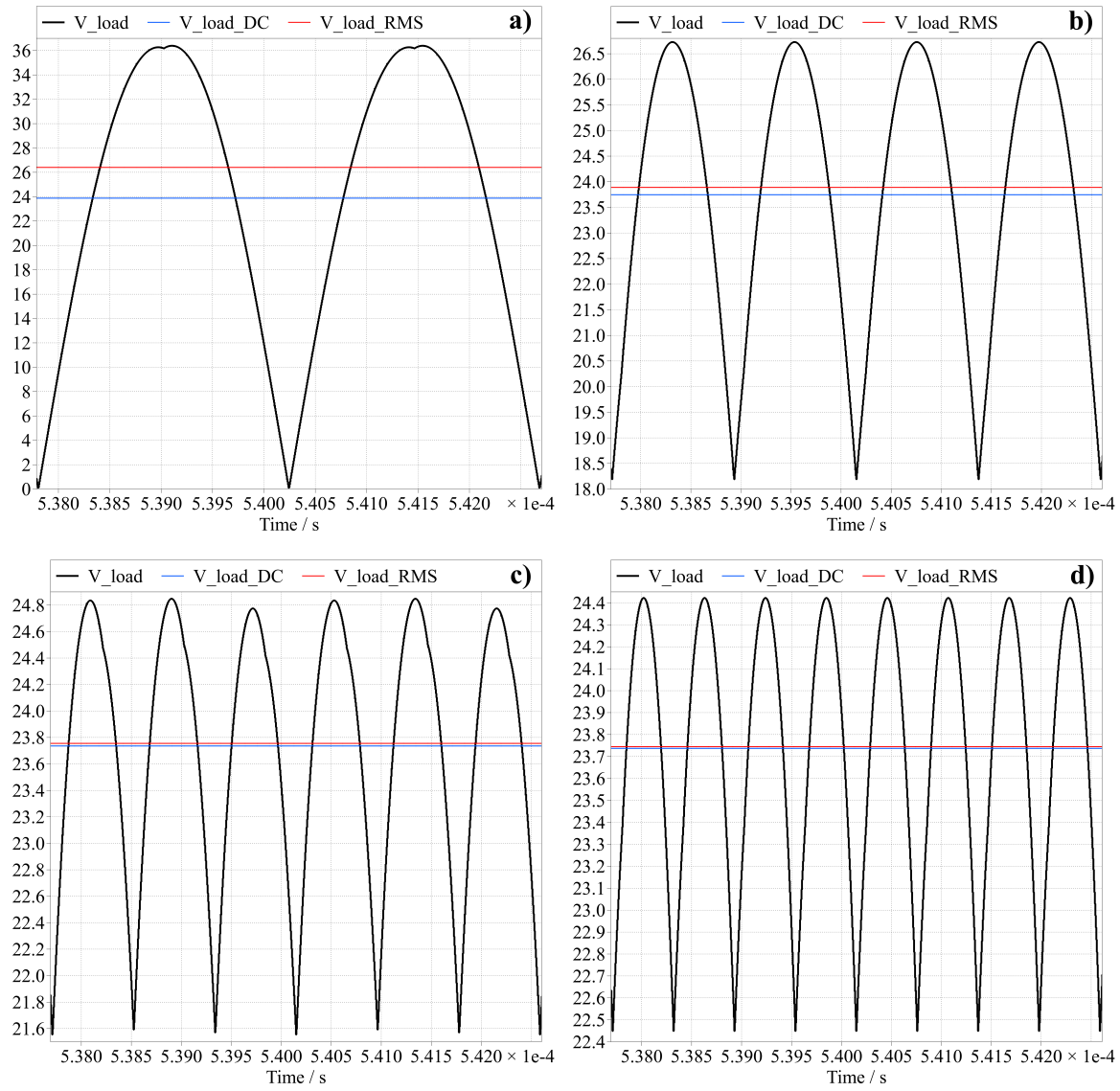

Figure 7.5: Instant voltage across the load in the case of half period equal displacement (HPED) with 1 (a), 2 (b), 3 (c) and 4 (d) modules. The DC and RMS voltage values are depicted as well.

Table 7.10: Half period equal displacement DC values.

$N_{modules}$	Firing signals	$V_{load,dc}$	$I_{load,dc}$	$P_{load,dc}$
2	[0 0.25]	23.7469 V	2.7210 A	65.3947 W
3	[0 0.167 0.33]	23.7357 V	4.0796 A	96.9900 W
4	[0 0.125 0.25 0.375]	23.7372 V	5.4398 A	129.2078 W

Table 7.11: Half period equal displacement RMS values.

$N_{modules}$	$V_{load,rms}$	$I_{load,rms}$	$P_{load,rms}$
2	23.8897 V	2.7374 A	66.8279 W
3	23.7552 V	4.0829 A	97.2983 W
4	23.7447 V	5.4415 A	129.3699 W

Table 7.12: Half period equal displacement ripple values.

$N_{modules}$	$V_{load,dc}$	$V_{load,max}$	$V_{load,min}$	$V_{load,delta}$	Ripple
2	23.7469 V	26.7272 V	18.1921 V	8.53510 V	0.35942
3	23.7357 V	24.8481 V	21.5552 V	3.2929 V	0.13873
4	23.7372 V	24.4224 V	22.4495 V	1.9729 V	0.08311

7.3 RD - Random Displacement

In the previous section, the best and worst cases from ripple and power perspectives were identified. The objective of this section is to provide a general overview of what happens to the system when the FSs are not controlled. For each module, a random number (r_p) from a uniform distribution with a lower limit of 0 and an upper limit of 1 is retrieved (PDF reported in Figure 7.6).

$$t_{firing} = r_p \cdot T \tag{7.4}$$

Then the instant of FS is calculated as expressed in Equation 7.4. Since this is a statistical study, the number of simulations performed is chosen according to Appendix B.

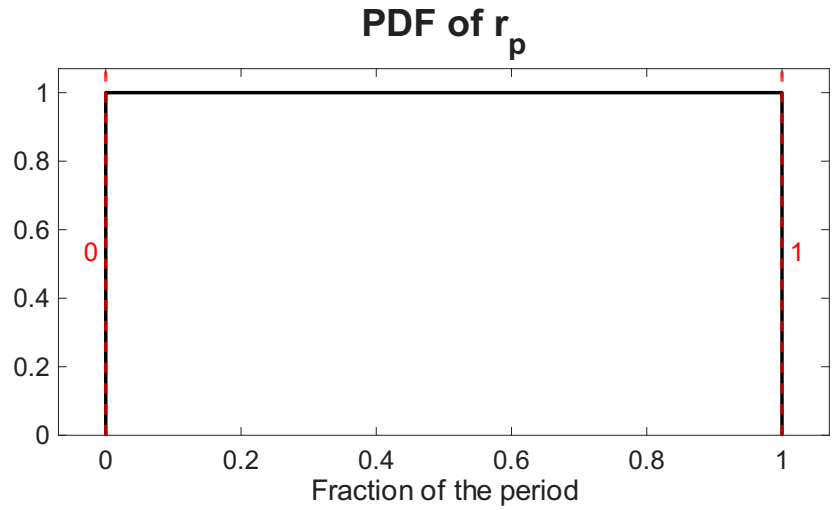

Figure 7.6: PDF of the uniform distribution for calculating the FSs for the RD study.

7.3.1 Relation between power and ripple

According to the reasoning reported in Appendix B, three batches of 6'000 simulations for 2, 3 and 4 modules were collected. Using the MATLAB script described in Section 6.2, an analysis was performed, resulting in:

- For all configurations, the maximum ripple ($\simeq 1.52$) and maximum DC power ($\simeq 40 \cdot N_{modules}$ W) is the one resulting from ND described in Subsection 7.2.1.
- The minimum ripple and DC power is the one resulting from HPED described in Subsection 7.2.3 for 2 modules (ripple $\simeq 0.36$, DC power $\simeq 66$ W) and 4 modules (ripple $\simeq 0.08$, DC power $\simeq 129$ W), and from ED (or HEPD as well) described in Subsection 7.2.2 for 3 modules (ripple $\simeq 0.14$, DC power $\simeq 97$ W).

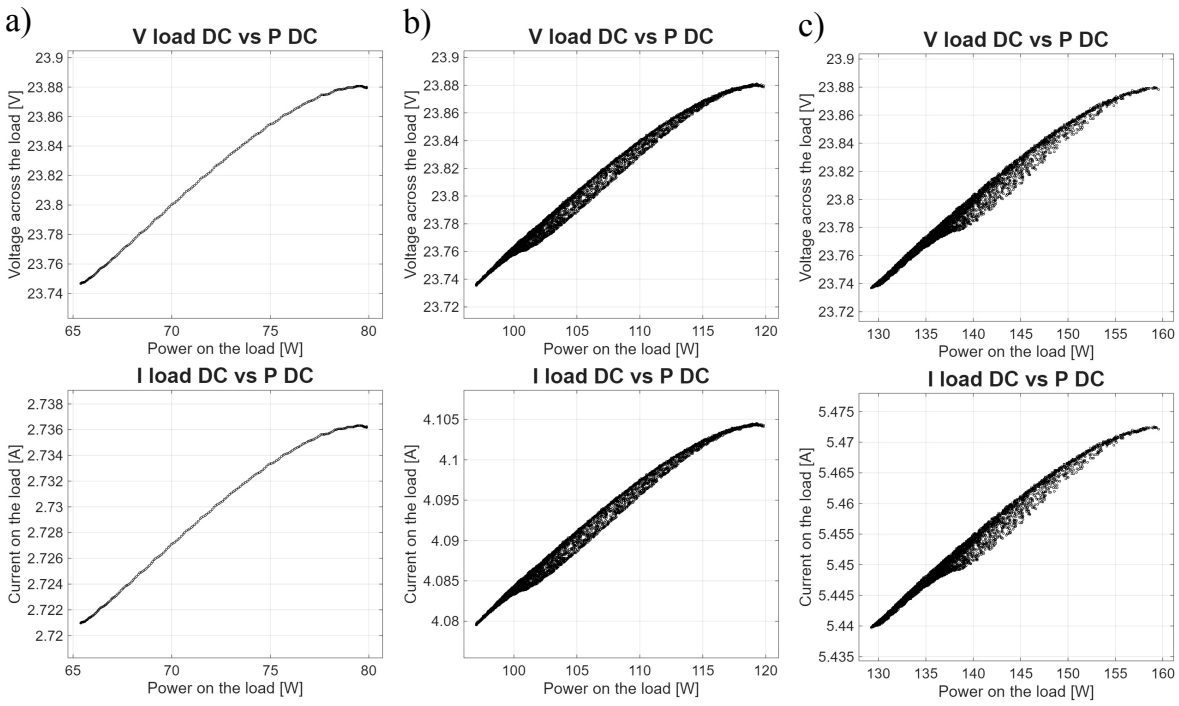

Figure 7.7: Trend's plots of the three main parameters of interest for 2 (a), 3 (b) and 4 (c) modules.

In Figure 7.8 are reported the plots of the output DC power normalized by the number of modules versus the ripple. A clear result is that the behavior of the system does not change in changing the number of modules.

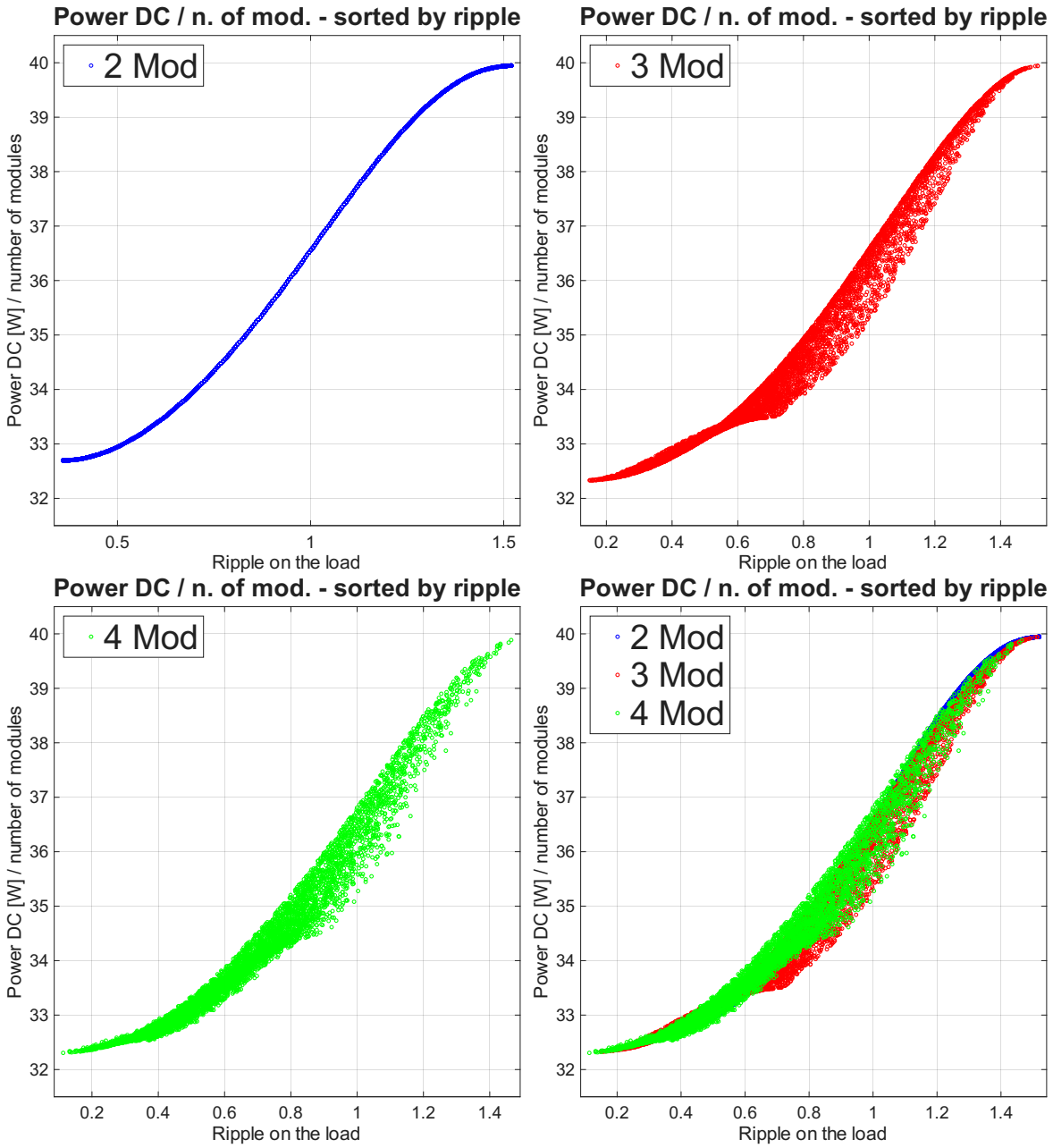

Figure 7.8: Output DC power normalized by the number of modules versus the ripple. Reporting the plots of 2, 3, 4 modules, and an overlay of all three cases.

7.3.2 PSI - Phase Shifting Index

Given the clear relationship between DC power and ripple, it would be interesting to develop a parameter to describe it. A good starting point is the proposed Phase Shifting Index (PSI). It is the summation of the relative distances between the FSs. PSI works perfectly describing the system composed of 2 modules as shown in Figure 7.10, but due to the problem described at the end of this subsection, it does not describe unequivocally the power DC-ripple relationship in the case of 3 and 4 modules. In the following is described the calculation of PSI:

1. Bring all the FSs in the interval [0 0.5]. The diagonals of the H-Bridge are working with a duty cycle of 0.5, adding also the action of FWR (Figure 7.9), it is possible to bring all the FSs in the interval [0 0.5] without losing information on the relative displacement between the modules. This makes the calculation of PSI easier because a displacement of 0, 0.5 or 1 has the same result.

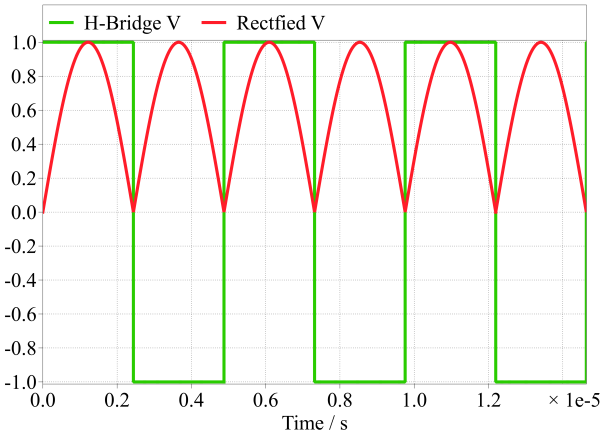

Figure 7.9: Graphical representation of the full wave rectifier action.

2. Sort in ascending order the FSs;

3. Take the lowest FS (FS_r) as reference and calculate the summation of all the others;

$$SUM = \sum_{i=2}^{numMod} FS_i - FS_r \tag{7.5}$$

4. Normalize as in Formula 7.6, obtaining the PSI. The normalization is applied for two main reasons: to always obtain a value in the interval [0 0.5] and to allow comparing systems with different numbers of modules.

$$PSI = \frac{\sum_{i=2}^{numMod} FS_i - FS_r}{numMod - 1} \tag{7.6}$$

In Figure 7.10, the trend of PSI describing a system composed of 2 modules is shown. The result is completely in line with the discussion in Subsection 7.3.1.

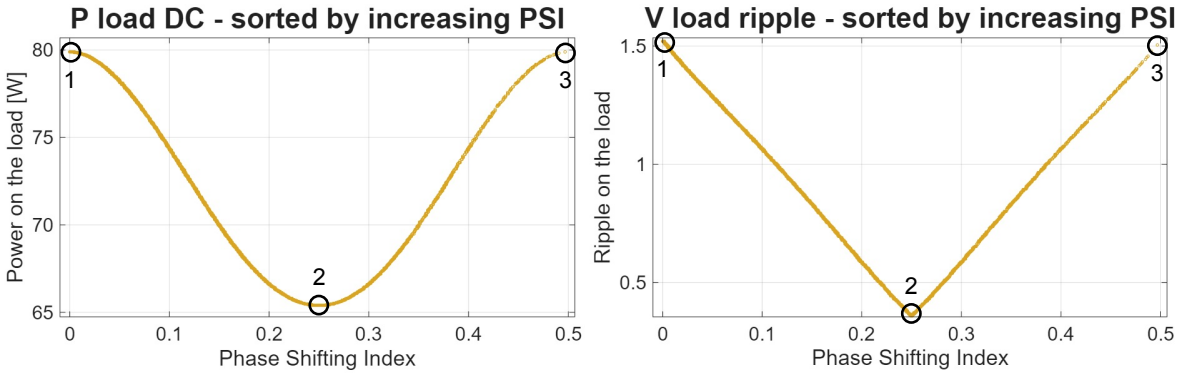

Figure 7.10: DC Power versus PSI and voltage ripple versus PSI in a system composed of 2 modules.

In fact, at the points:

1. Firing of module 1 and 2 happens at the same instant. As expected resulting in both maximum DC power and ripple.

2. The modules work at [0 0.25], as described in the HPED Subsection 7.2.3, both power DC and ripple are at minimum.

3. Firing of module 1 is displaced by half period with respect to module 2. Due to the action of FWR, this configuration is equivalent to ND. As in point 1, resulting in maximum DC power and ripple.

PSI - The Problem

As shown, PSI is working egregiously for a system of 2 modules. Unfortunately, the given definition does not apply well to the cases of 3 and 4 modules. This is because PSI is not unequivocally linking displacement and behavior of the system (this problem is graphically described in Figure 7.12). In the 2-modules system, there is only 1 degree of freedom, so the calculation is correct. Instead for a system with 3 modules, there are 2 degrees of freedom, and in the case of 4 modules, 3 degrees of freedom, resulting in the impossibility to describe the behavior with only one parameter. Nevertheless, the plots depicted in Figure 7.11 are promising because they follow the same trend as the 2-modules case.

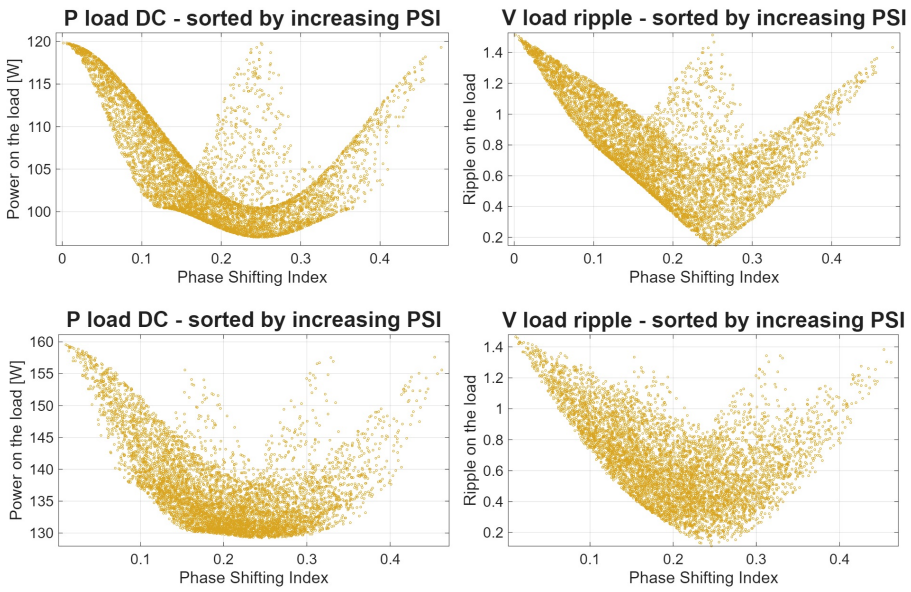

Figure 7.11: DC Power versus PSI and voltage ripple versus PSI for a system composed of 3 modules (up) and 4 modules (down).

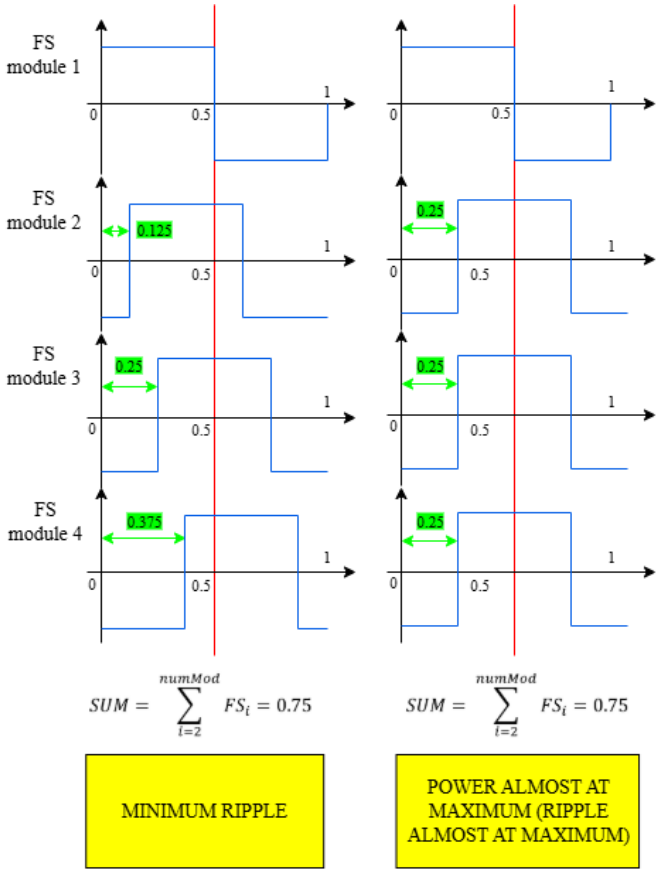

Figure 7.12: PSI's problem of lack of univocity in linking displacement and behavior of the system

Chapter 8

Uncertainty on the Compensation Capacitances

The present chapter aims at quantifying how, and how much, the uncertainties on the components of the IPT coupler affect the overall efficiency and functionality of the system. As the restricted variation on the inductances has a limited impact [52], the parameters selected for the uncertainty quantification are chosen to be the capacitance values of the compensation capacitors. As is widely known in practice, the tolerances on the values of the capacitors commercially available are equal to ±20%, but higher quality and more expensive realizations can offer uncertainties of ±10% or ±5%. In [53] and [54], some datasheets of several capacitors produced by *KEMET Corporation* and *Alcon Electronics* have been analyzed. As stated, the typical value of tolerances on the value of the capacitance is, indeed, ±20%, ±10% and ±5%. With a view to the worst case scenario, the variation of the capacitance is imposed at ±20% of the target value as reported in Table 8.1.

Table 8.1: Boundaries value of the capacitances' variation.

	Target	**Lower boundary (80%)**	**Upper boundary (120%)**
C_{tr}	12.6 nF	10.1 nF	15.1 nF
C_{re}	25.1 nF	20.1 nF	30.1 nF

To study the impact of capacitance uncertainty on the system's behavior, uniform and normal distributions were chosen. The uniform distribution is used to have a clear idea of all types of configurations; instead, the normal distribution is used to assess the impact of a realistic distribution of capacitances' values. The study starts by calculating the parameters of the distributions, reported in Tables 8.2 and 8.3. In addition, the simulations will be performed under fixed displacement. ND for studying the maximum output DC power and HEPD for studying the worst output DC power case.

The presented results refer to a batch of simulations performed with a system composed of 4 modules. Since this is a statistical study, the number of simulations performed is chosen according to Appendix B.

8.1 Uniform distribution

The use of a uniform distribution allows testing all values of capacitance between the boundaries to understand how different configurations impact the system. The distribution parameters for both C_{tr} and C_{re} are listed in Table 8.2, and the probability density functions are plotted in Figure 8.1.

Table 8.2: C_{tr} and C_{re} uniform distributions parameters.

	Central value	**Lower limit (a)**	**Upper limit (b)**
C_{tr}	12.6 nF	10.1 nF	15.1 nF
C_{re}	25.1 nF	20.1 nF	30.2 nF

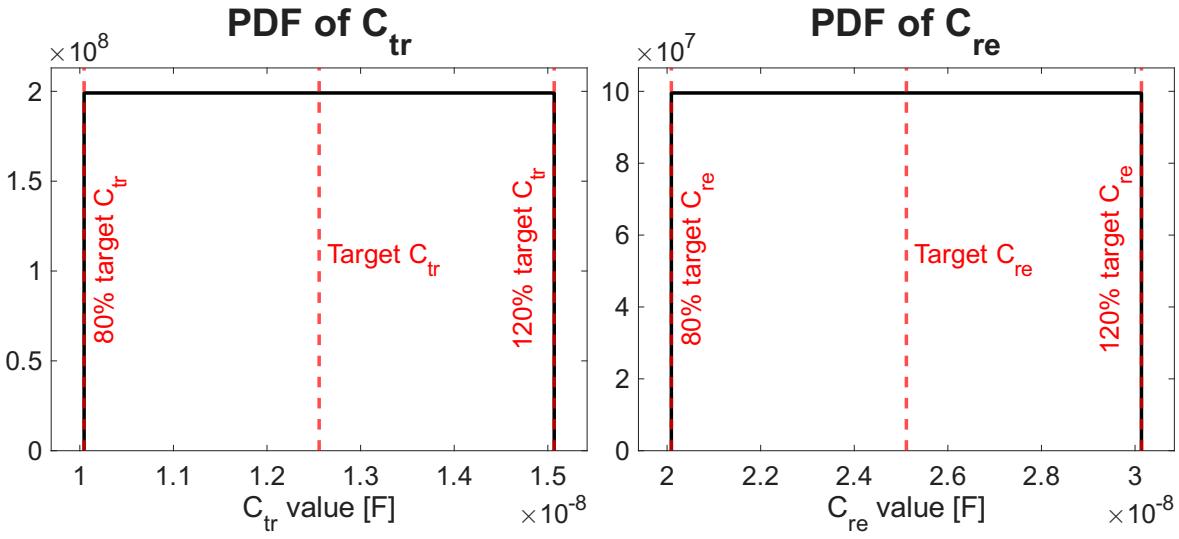

Figure 8.1: C_{tr} and C_{re} uniform distributions' PDFs.

In Figure 8.2, the behavior of single module output power (SMOP) DC varying C_{tr} and C_{re} is reported (both under ND and HEPD). As shown in 8.2 (b), the change of receiving compensation capacitance does not have a decisive impact on the SMOP DC. Instead, the change in the transmitting compensation capacitance determines a huge power variation (this aspect will be analyzed in Section 8.3). At target C_{tr}, the output power oscillates around the SMOP DC value ($\simeq$ 40 W from Section 7.1). On the right of target C_{tr} (value higher than the target), the SMOP DC is lowered slightly, but not significantly.

On the contrary, on the left of target C_{tr} (value lower than the target), the impact is huge, as the C_{tr} lowers, the SMOP DC plummets. It is worth noting that there are configurations where some modules contribute practically nothing to power transmission.

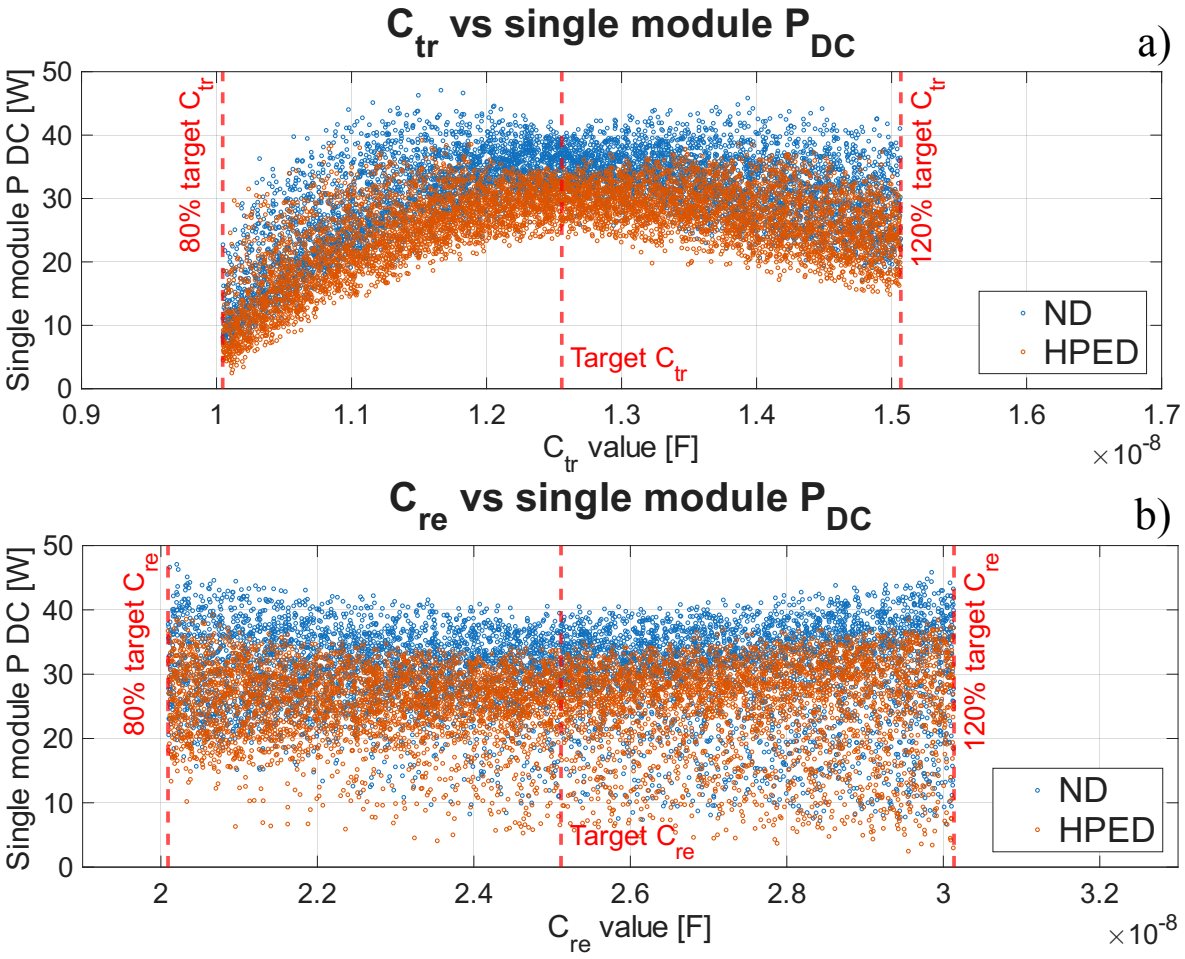

Figure 8.2: Variation of the SMOP DC in the change of transmitting (a) and receiving (b) compensation capacitances in the case of uniform distribution. Both ND and HPED cases are depicted.

The same trend can be highlighted in Figures 8.3 and 8.4. In Figure 8.3, the tridimensional plot of C_{tr} versus C_{re} versus SMOP DC is depicted.

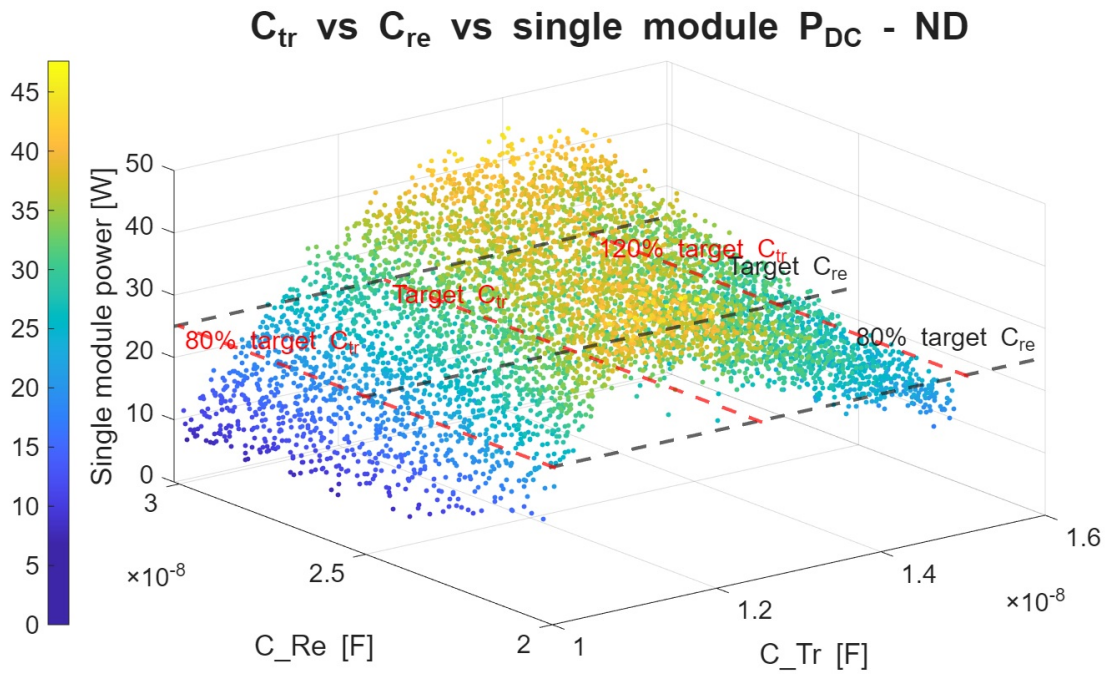

Figure 8.3: Transmitting capacitance versus receiving capacitance versus SMOP DC tridimensional graph in the case of uniform distribution and under ND.

In Figure 8.4 the perspective from the top of Figure 8.3 is given. It is evident that there is a central area where the power is higher (even greater than the case of the single module under ND, Section 7.1) and slowly fading toward the edges.

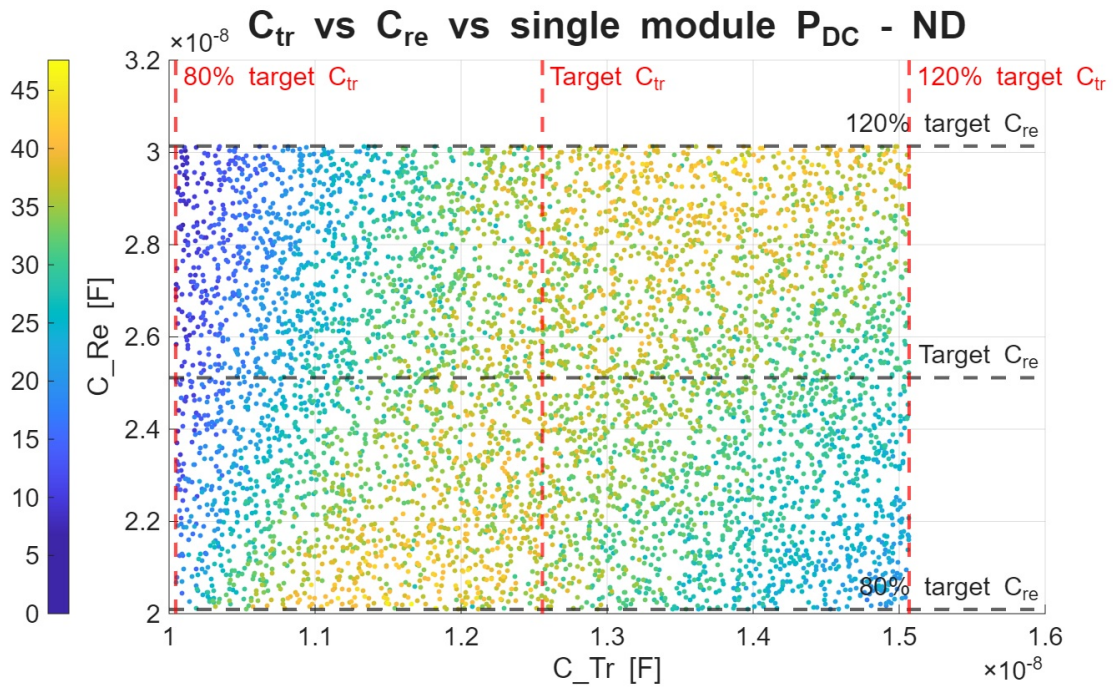

Figure 8.4: Transmitting capacitance versus receiving capacitance versus SMOP DC bi-dimensional graph in the case of uniform distribution and under ND.

In Figure 8.5 are reported the same plots as Figures 8.3 and 8.4 but in the case of HEPD. There are no changes in the system's behavior with respect to ND, but the SMOP DC is generally lower.

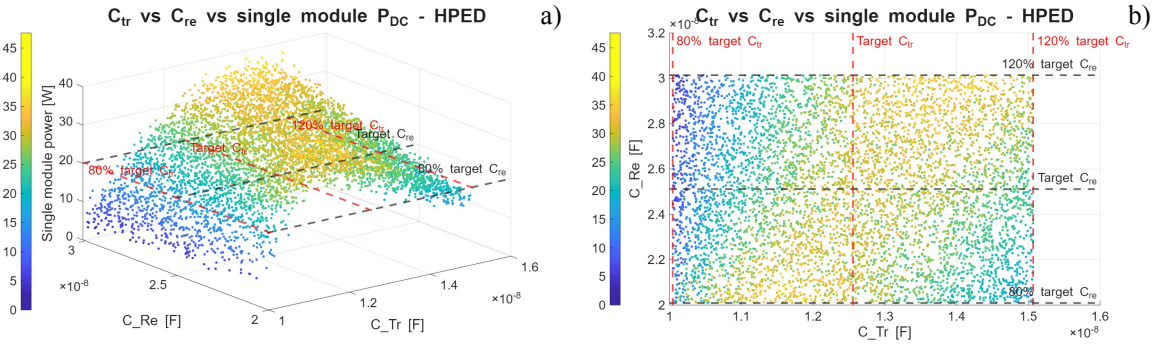

Figure 8.5: Transmitting capacitance versus receiving capacitance versus SMOP DC plots in the case of uniform distribution under HPED. a) Tridimensional graph. b) Bi-dimensional graph.

8.2 Normal distribution

In this section, the normal distribution is used to assess the impact of a realistic distribution of capacitances' values. Being the two distributions imposed, the calculation of the parameters (reported in Table 8.3) is straightforward. As expected values $\mu_{tr,re}$, target values C_{tr} and C_{re} are used (Equation 8.1). The standard deviations $\sigma_{tr,re}$ are calculated by imposing the boundaries of Table 8.1 to a cover factor of 3. In Figure 8.6, the PDFs are depicted.

Table 8.3: Normal distribution parameters.

	Expected value	**Standard deviation**	**Variance**
	μ	σ	σ^2
C_{tr}	12.6 nF	8.3713e-10 F	7.0079e-19 F^2
C_{re}	25.1 nF	1.6743e-09 F	2.8032e-18 F^2

Where:

$$\mu_{tr,re} = C_{tr,re,target} \tag{8.1}$$

$$\sigma_{tr,re} = \frac{1.2 \cdot C_{tr,re} - \mu_{tr,re}}{3} = \frac{\mu_{tr,re} - 0.8 \cdot C_{tr,re}}{3} \tag{8.2}$$

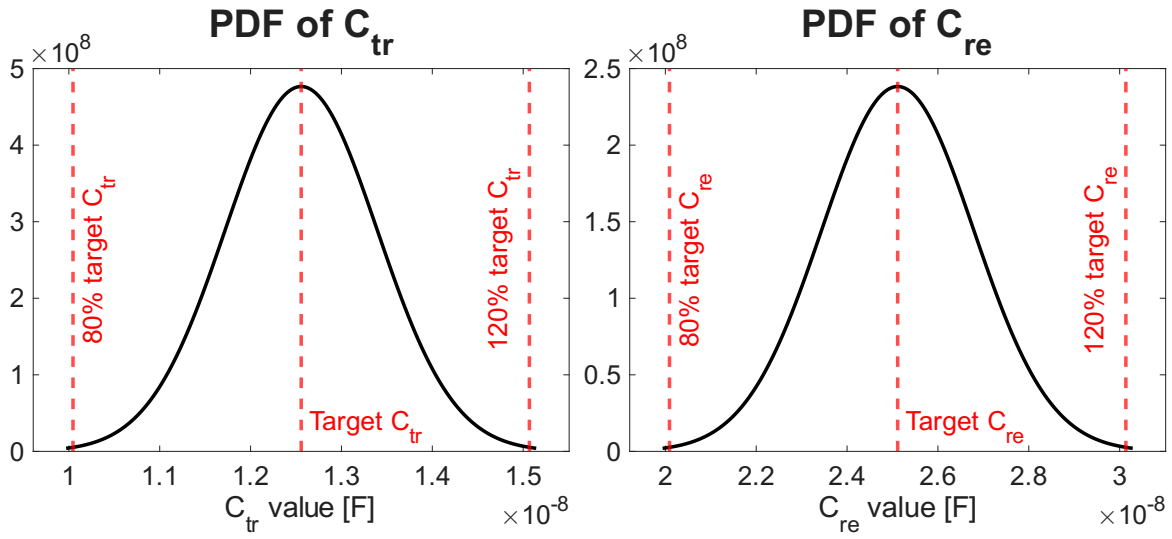

Figure 8.6: C_{tr} and C_{re} normal distributions' PDFs.

In Figures 8.7, 8.8, 8.9 and 8.10, the same plots as the previous section, but imposing a normal distribution for the compensation capacitances, are reported. Except for the clustering around the target capacitances' values, there are no other substantial differences.

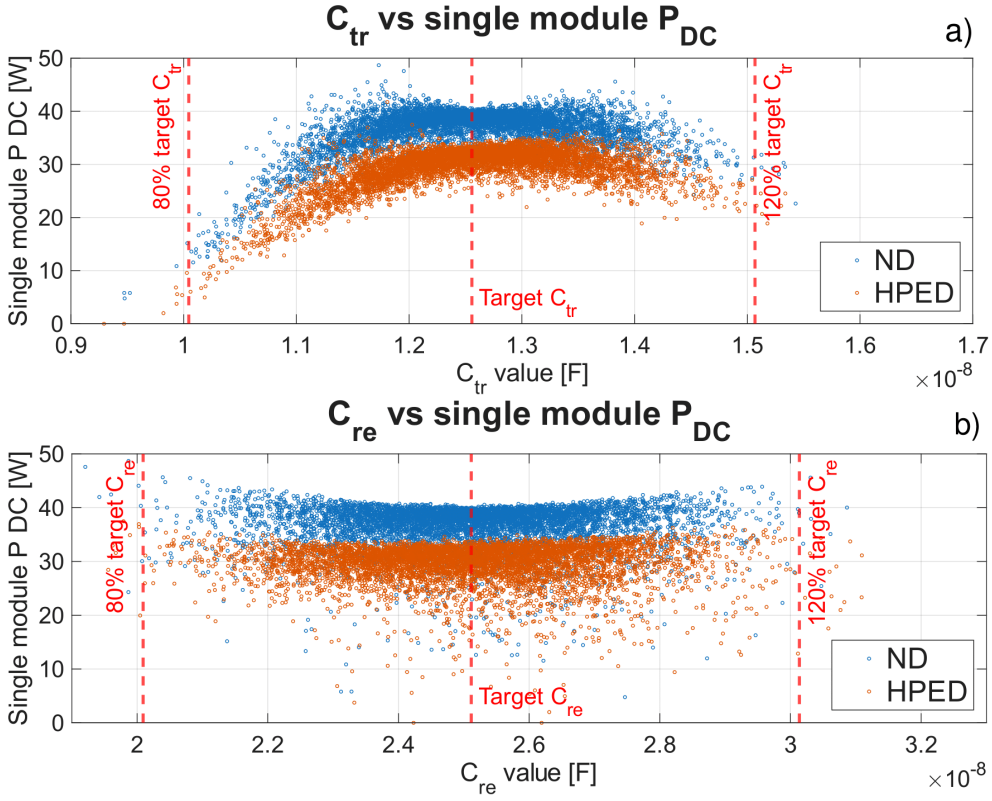

Figure 8.7: Variation of the SMOP DC in the change of transmitting (a) and receiving (b) compensation capacitances in the case of normal distribution. Both ND and HPED cases are depicted.

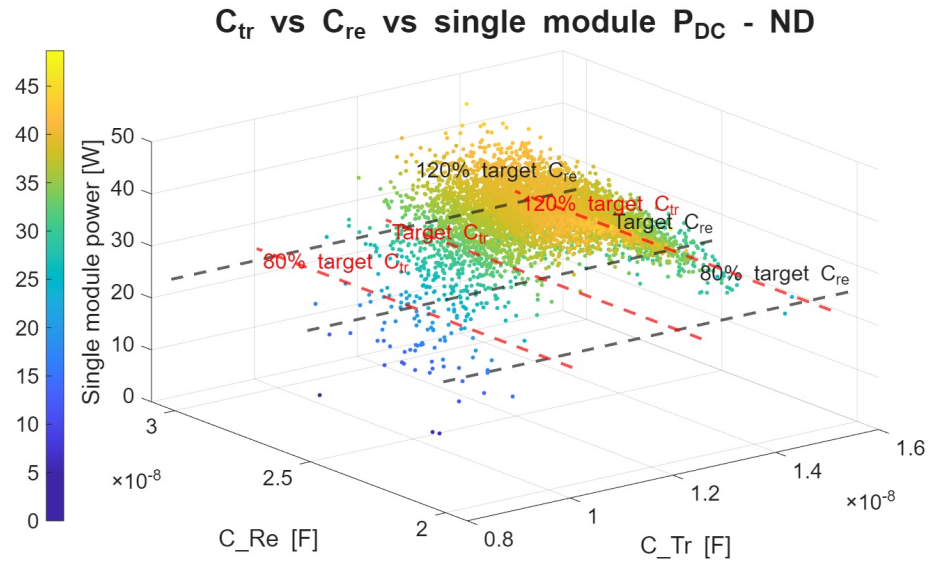

Figure 8.8: Transmitting capacitance versus receiving capacitance versus SMOP DC tridimensional graph in the case of normal distribution and under ND.

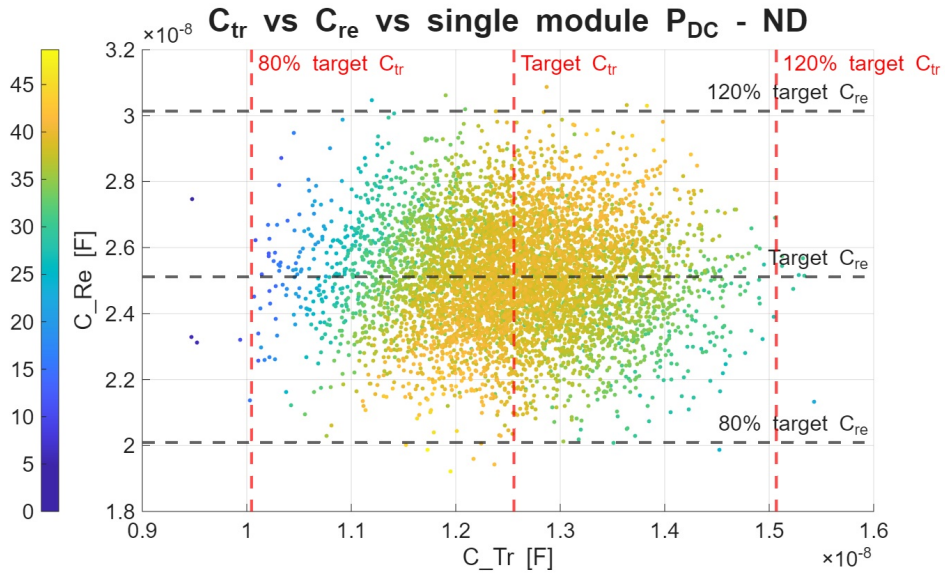

Figure 8.9: Transmitting capacitance versus receiving capacitance versus SMOP DC bi-dimensional graph in the case of normal distribution and under ND.

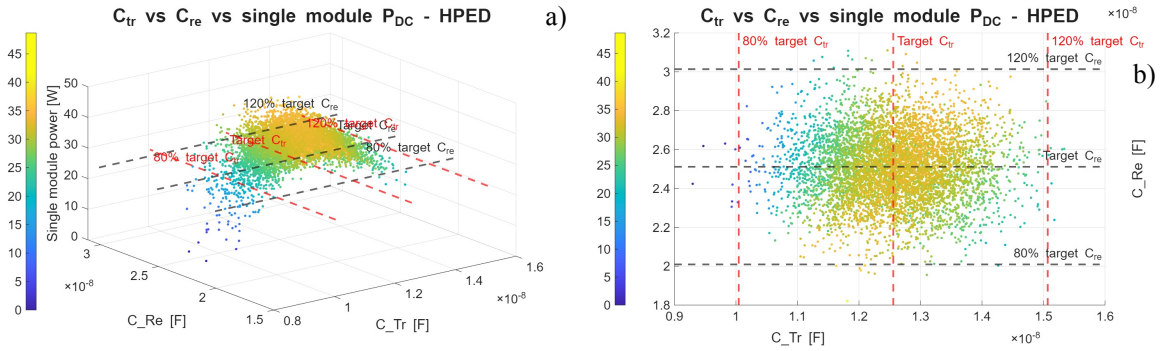

Figure 8.10: Transmitting capacitance versus receiving capacitance versus SMOP DC plots in the case of normal distribution and half period equal displacement. a) Tridimensional graph. b) Bi-dimensional graph.

8.3 Conclusive analysis and explanation proposal

Based on the data collected from the simulations described in the previous section is possible to draw conclusions and propose an explanation to the highlighted trends. As first step, the highest and lowest SMOP DC obtained from the simulations are reported in Table 8.4.

Table 8.4: Lowest and highest SMOP DC resulting from the reported C_{tr} and C_{re} configurations. Delta percentage is calculated as well.

	Lowest SMOP DC	**Highest SMOP DC**
C_{tr}	10.11 nF	11.66 nF
C_{re}	29.55 nF	20.20 nF
SMOP DC	2.478 W	47.08 W
Δ%SMOP DC	-93.8%	+17.8%

The difference between the two is huge, the delta percentage is calculated as Δ%SMOP DC = (SMOP DC/$P_{load,dc} - 1) \cdot 100$, where $P_{load,dc}$ is the power of the single module from Section 7.1.

8.3.1 Impact of the variation of C_{tr} and C_{re} on $\overline{Z_T}$

To understand how the system behaves in varying the compensation capacitances values is useful to plot the modulus and the phase of the total output impedance $\overline{Z_T}$ from Formula A.7. In Figure 8.11 the impact of both C_{tr} and C_{re} on $\overline{Z_T}$ is depicted.

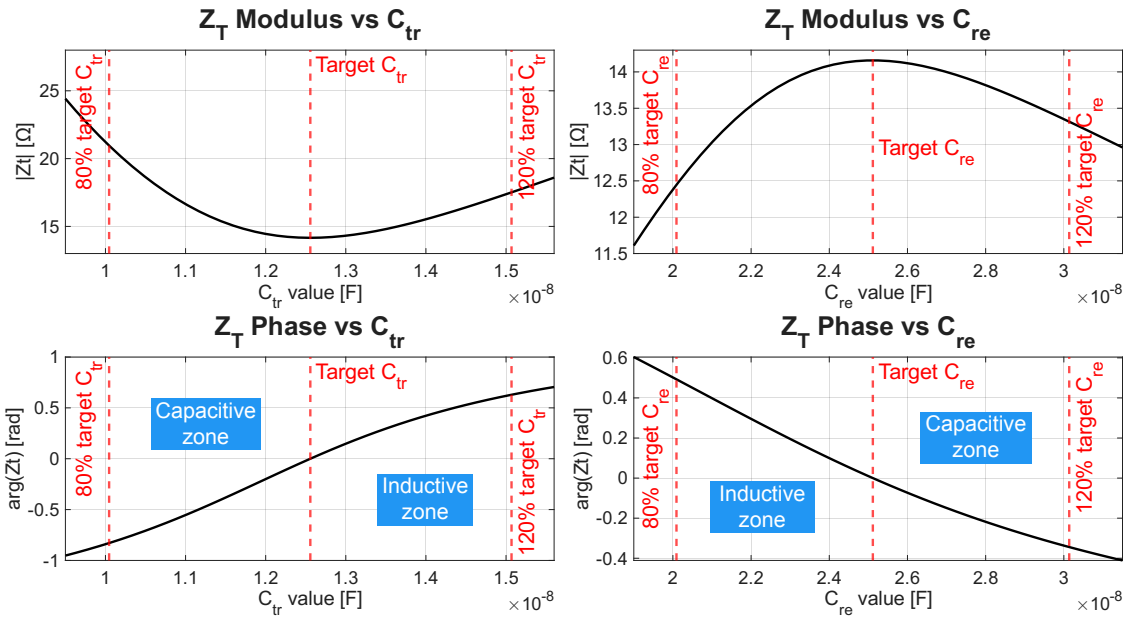

Figure 8.11: Behavior of $|\overline{Z_T}|$ and arg($\overline{Z_T}$) in varying C_{tr} and C_{re}.

In Table 8.5 are reported the numeric values of modulus and phase of $\overline{Z_T}$ at target, lower boundary, and upper boundary of compensation capacitances values. The percentage variation with respect to resonance condition are reported as well. The change in C_{tr} implicates a major variation of both $|\overline{Z_T}|$ and $\arg(\overline{Z_T})$. This results in a more pronounced impact as shown in Figures 8.2 and 8.7. In particular, when C_{tr} becomes lower than the target, $\arg(\overline{Z_T})$ becomes negative, so capacitive. The switching action on a capacitive load involves managing the inrush current that occurs when a capacitor is charged or discharged. When a capacitive load is switched on, a high inrush current flows as the capacitor charges. This current can be significantly larger than the steady-state current and potentially damage the switching device.

Table 8.5: Total output impedance numeric values at target, lower boundary, and upper boundary of compensation capacitances values. The percentage variation are referred to the target value.

	Lower boundary	**Target**	**Upper boundary**
$\lvert\overline{Z_T}\rvert$ vs C_{tr}	20.91 Ω (+47.67%)	14.16 Ω \	17.52 Ω (+23.73%)
$\arg(\overline{Z_T})$ vs C_{tr}	-0.8270 rad (capacitive)	0 rad (resonance)	0.6255 rad (inductive)
$\lvert\overline{Z_T}\rvert$ vs C_{re}	12.46 Ω (-12.01%)	14.16 Ω \	13.33 Ω (-5.862%)
$\arg(\overline{Z_T})$ vs C_{re}	0.4891 rad (inductive)	0 rad (resonance)	-0.3418 rad (capacitive)

In Figure 8.12 is reported the bi-dimensional graph C_{tr} versus C_{re} versus SMOP DC under the same conditions of 8.4 but representing only the configurations resulting in SMOP DC greater than 33 W. This value is chosen because the target output power from Chapter 4 is 33 W, and since the implementation on PLECS does not present dissipation, if the power SMOP DC become lower than 33 W, that value would not be achivable for sure in a realistic implementation. The behavior of the system is clear, as soon as the variation of both compensation capacitances is such that their impact on the total output impedance mitigates each other (shifting towards positive and negative phase from plot 8.11), SMOP DC does not undergo major changes.

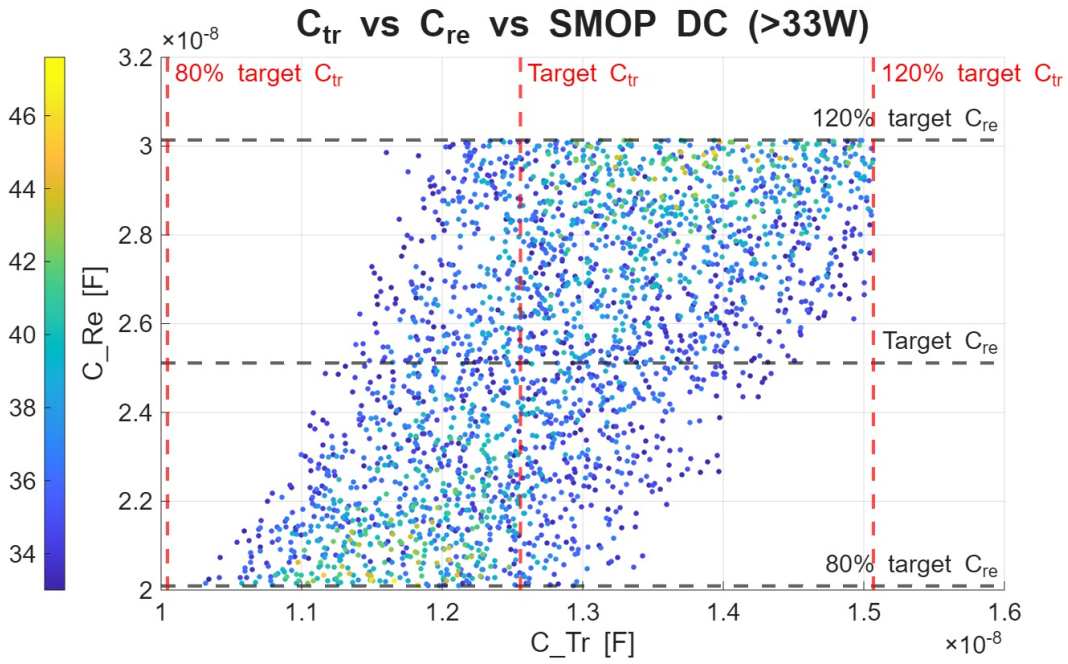

Figure 8.12: C_{tr} versus C_{re} versus SMOP DC bi-dimensional graph under the same conditions of 8.4 but representing only the configurations resulting in SMOP DC greater than 33 W.

8.3.2 Mitigation of uncertainty impact by frequency shifting

As expressed in Equation A.1, the resonance frequency of a series-series IPT system depends (only) on the compensation capacitances' values. Assuming to know the variation of C_{tr} and C_{re} (one at a time), to nullify the impact of this change, it is possible to properly shift the working frequency. Employing this technique results in the mitigation of the impact of the uncertainty on the system.

Table 8.6: Summary of the values of interest in performing frequency shifting. The percentage variation are referred to the target value.

	Lower boundary	**Target**	**Upper boundary**
L_{tr}	48 µH	48 µH	48 µH
L_{re}	24 µH	24 µH	24 µH
C_{tr}	10.1 nF	12.6 nF	15.1 nF
C_{re}	20.1 nF	25.1 nF	30.2 nF
ΔC_{tr}	2.51 nF	/	2.51 nF
ΔC_{re}	5.02 nF	/	5.02 nF
f_{res}	229.2 kHz	205 kHz	187.2 kHz
Δf_{res}	24.2 kHz	/	17.9 kHz
$\Delta\% f_{res}$	+11.8%	/	-8.68%

Chapter 9

Conclusion and Future Works

The advent of autonomous vehicles marks a new frontier of innovation. Moved from the growing interest in drones because of their ability to quickly, accurately, and unobtrusively move in three dimensions, they are studied in depth in this work. Drones are particularly useful in applications that reduce risk for human operators, such as rescue missions, fighting forest fires, and structural inspections.

However, to fully leverage the cooperative and autonomous functionalities of UAV employing systems, it is critical to address and optimize their energy management strategies. In fact, their major drawback is the short flight time.

This final work has explored the design, analysis, and simulation of a modular series-series compensated Inductive Power Transfer charging system tailored for drone applications. Starting from the investigation of Wireless Power Transfer principles, WPT historical and technological evolution, and consequently the state of the art, the work has highlighted the importance of efficient and autonomously charging solutions in the rapidly expanding field of Unmanned Aerial Vehicles.

A detailed market analysis of drones was conducted to identify key electrical and mechanical aspects, common trends, and constraints, such as materials, voltage levels, power levels, and charging requirements. This information has driven the design requirements for the proposed IPT system. By adopting a modular approach, this work successfully addresses the Qi v2.0 standard limitations. Additionally, the modular approach enables power scalability and enhances system redundancy and fault tolerance.

The coils' design phase, carried out following guidelines found in literature and analytical calculations, led to the development of an efficient inductive coupler composed of a transmitting coil with radius 30 mm and a receiver coil with radius 50 mm, both employing a ferrite disk. This solution offers favorable tolerance to misalignment and can achieve the required power output. The subsequent review of commercially available coils analyzed by means of FEMM magnetic simulations confirmed the viability of market-ready coils as alternatives to more onerous, built-from-scratch solutions.

To fully understand the behavior of the system under test, an interconnected and cooperative environment made up of Plexim PLECS, MathWorks MATLAB and Mi-

crosoft Excel was designed. The PLECS implementation takes as input the characterizing (and imposed) parameters of the specific simulation to perform, calculates the remaining parameters, performs the electrical circuit simulations, and exports the results as MATLAB MAT-files. Thereafter, MATLAB is employed to organize, analyze and build reports consisting of graphs and Microsoft Excel tables. As last resort, Microsoft Excel is used to access the reports and as a fast check for consistency of results.

The personalized implementation from scratch in PLECS enabled accurate characterization of system behavior (with focus on power transfer and voltage across the load ripple) under various fixed (No Displacement, Equal Displacement, Half-Period Equal Displacement) and Random displacements between the modules scenarios. Another aspect under study has been the quantification of the impact of uncertainties on compensation capacitance. Trends, best, and worst working points were discovered through an experimental approach sustained by a solid 90'000 simulations batch. These simulations revealed that both the displacement of modules and the compensation capacitances uncertainty significantly affect power stability and voltage across the load ripple.

This work lays the groundwork for future developments in automated drone charging infrastructure. The modular IPT charging system proposed in this work has the potential to significantly enhance the autonomy and operational efficiency of future drone fleets.

9.1 Highlights of this work

The following is a bulleted list to sum up the results of this study:

- The lack of control of the FSs (RD, Section 7.3) leads the system to behave too differently in the best (ND, Subsection 7.2.1, under power perspective and HPED, Subsection 7.2.3, under voltage ripple perspective) and worst (HPED under power perspective and ND under voltage ripple perspective) cases. A control strategy is required.

- In case an FSs control system is implemented, it can be operated to pursue different goals. Imposing a fixed ND in case the goal is to maximize power, or a fixed HPED in case minimizing the ripple is the objective.

- Even in the best scenario, the system composed of 4 modules under HPED (Subsection 7.2.3), which results in a voltage ripple $\simeq 8\%$, this value is not acceptable for charging a battery. As stated in *IEEE 2405-2022 - Standard for the Design of Chargers Used in Stationary Battery Applications* [55] for a battery of 24 V the *minimum filter level* is set to 2% Vrms and the *high filter level* is set to 30 mV on Vrms. Concluding that an output capacitor filter is needed.

- In an ideal scenario, where the compensation capacitances are varying one at a time and the change can be known, the impact of the uncertainty of the capacitances can be limited by shifting the working frequency (Subsection 8.3.2). Anyway, as a result of Section 8.2, if the uncertainty on capacitances is certified to be a normal distribution (or higher quality capacitors offering uncertainties of $\pm 10\%$ or $\pm 5\%$ are employed), it would barely have any impact on the system.

9.2 Proposed upcoming developments

As the last topic of this work, some suggestions are left for future developments aimed at deepening and improving the work:

- Improving the PSI (Subsection 7.3.2), a matrix approach might be the solution? Where ϕ_1, ϕ_2, ϕ_3 and ϕ_4 are the FSs.

$$M_{PSI} = \begin{bmatrix} \phi_1 - \phi_1 & \phi_1 - \phi_2 & \phi_1 - \phi_3 & \phi_1 - \phi_4 \\ \phi_2 - \phi_1 & \phi_2 - \phi_2 & \phi_2 - \phi_3 & \phi_2 - \phi_4 \\ \phi_3 - \phi_1 & \phi_3 - \phi_2 & \phi_3 - \phi_3 & \phi_3 - \phi_4 \\ \phi_4 - \phi_1 & \phi_4 - \phi_2 & \phi_4 - \phi_3 & \phi_4 - \phi_4 \end{bmatrix} \tag{9.1}$$

- Explore the uncertainty on compensation capacitances' impact on the voltage across the load ripple, as done in Chapter 8 under the output power perspective.

- Experimental validation. Assembling a prototype of the proposed modular series-series IPT system to validate simulation outcomes and refine the design under real-world conditions.

- Safety and EMC compliance. Further analysis of electromagnetic compatibility and biological safety to ensure compliance with regulations for widespread deployment.

- Design path for the output filter capacitor. Propose a solution that simultaneously limits weight and adapts dynamically as the number of modules changes.

- Propose a better frequency shifting approach to mitigate the uncertainty on compensation capacitances' impact on the system.

Appendix A

IPT Series-Series Compensated Formulas

With reference to the schematic drawn in Figure A.1, the formulas (taken from the egregious work [27]) to calculate all parameters of interest are reported in this appendix.

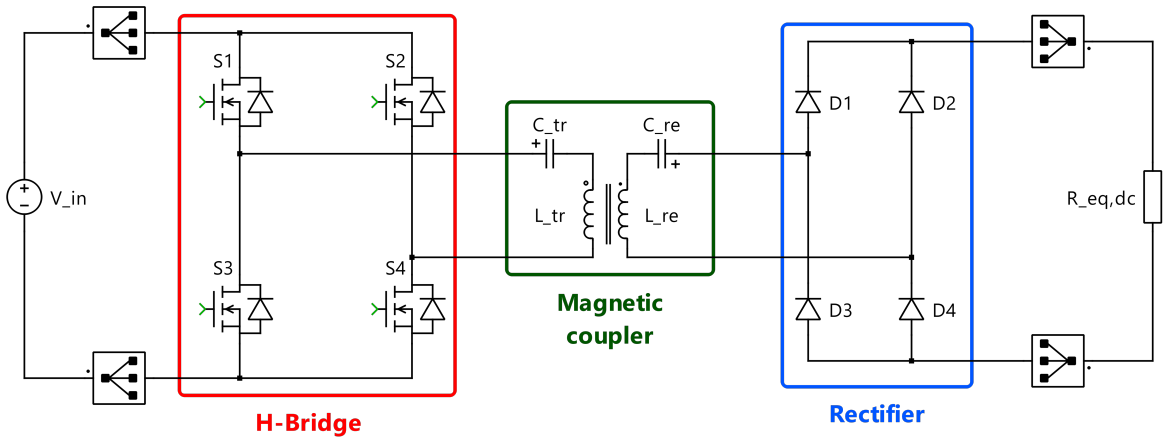

Figure A.1: Circuit representation of the chosen model.

Working pulsation or resonant pulsation.

$$\omega_0 = 2\pi f = \frac{1}{\sqrt{C_{tr} \cdot L_{tr}}} = \frac{1}{\sqrt{C_{re} \cdot L_{re}}} \tag{A.1}$$

DC load resistance.

$$R_{eq,dc} = \frac{V_{out}^2}{P_{SMO}} \tag{A.2}$$

Equivalent resistance value of $R_{eq,dc}$ brought back upstream of the rectifier.

$$R_{eq,ac} = \frac{8}{\pi^2} R_{eq,dc} \tag{A.3}$$

Transmitting compensation capacitance.

$$C_{tr} = \frac{1}{\omega_0^2 \cdot L_{tr}} \tag{A.4}$$

Receiving compensation capacitance.

$$C_{re} = \frac{1}{\omega_0^2 \cdot L_{re}} \tag{A.5}$$

Mutual inductance.

$$M = \frac{\sqrt{R_{eq,ac} \cdot Z_T}}{\omega_0} = k\sqrt{L_{tr} \cdot L_{re}} \tag{A.6}$$

Total output impedance (neglecting coils' resistance).

$$\overline{Z_T} = j \cdot \left(\omega_0 \cdot L_{tr} - \frac{1}{\omega_0 \cdot C_{tr}}\right) + \frac{\omega_0^2 \cdot M^2}{R_{eq,ac} + j\left(\omega_0 \cdot L_{re} - \frac{1}{\omega_0 \cdot C_{re}}\right)} \tag{A.7}$$

Modulus of the total output impedance calculated at resonant pulsation (neglecting coils' resistance).

$$Z_T = |\overline{Z_T}|_{\omega 0} = \frac{\omega_0^2 \cdot M^2}{R_{eq,ac}} = \left(\frac{4 \cdot V_{in}}{\pi \cdot \sqrt{2}}\right)^2 \cdot \frac{1}{P_{SMO}} \tag{A.8}$$

Coupling coefficient.

$$k = \frac{M}{\sqrt{L_{tr} \cdot L_{re}}} \tag{A.9}$$

Transmitting quality factor.

$$Q_{tr} = \frac{R_{eq,ac} \cdot L_{tr}}{\omega_0 \cdot M^2} \tag{A.10}$$

Receiving quality factor.

$$Q_{re} = \frac{\omega_0 \cdot L_{re}}{R_{eq,ac}} \tag{A.11}$$

Appendix B

Reasoning on Number of Simulations

When it is time to perform simulations, the question of how many samples to collect arises. The goal of this appendix is to provide a general guideline. First, in this work, the probability distribution from which the random values are taken is imposed. Consequently, as the parameters are known in advance, formula B.4 can be utilized. In the following, the explanation of this formula is presented.

Mathematically, when estimating the population mean using an independent and identically distributed sample of size n, where each data value has variance σ^2, the standard error e is:

$$e = \frac{\sigma}{\sqrt{n}} \tag{B.1}$$

This expression emphasizes how the error in estimating the mean value decreases as the sample size increases. Using the *central limit theorem* to justify approximating the sample to a normal distribution yields to expression of the confidence interval in the form:

$$\left(\bar{x} - \frac{Z \cdot \sigma}{\sqrt{n}},\ \bar{x} + \frac{Z \cdot \sigma}{\sqrt{n}}\right) \tag{B.2}$$

Where $\bar{x}$ is the true mean value, Z is a standard Z-score for the desired level of confidence (1.96 for a 95% confidence interval). Given a confidence interval of width W, so $W/2$ as the margin of error on each side of the sample mean and imposing it in Equation B.2:

$$\frac{Z \cdot \sigma}{\sqrt{n}} = \frac{W}{2} \tag{B.3}$$

Finally making n explicit from equation B.3:

$$n = \frac{4 \cdot Z^2 \cdot \sigma^2}{W^2} \tag{B.4}$$

The parameters Z and σ in Equation B.4 are imposed, so the only degree of freedom is W, which can be easily calculated from an imposed margin of error (expressed as % of the mean).

Another crucial aspect in performing heavy simulations is the time required. The developed PLECS model running on an average modern personal computer takes approximately 0.04 minutes (2.4 seconds) for each simulation to perform. In Table B.1 is reported an overview of all the aforementioned parameters with varying margin of error.

Table B.1: Number of simulations and total time required with varying margin of error.

Margin of error (% of the mean)	**Confidence interval width (W)**	**Batch size (n)**	**Total simulation time (min)**
1	5.02e-8	$\simeq$ 171	$\simeq$ 7
0.5	2.51e-10	$\simeq$ 683	$\simeq$ 28
0.25	1.26e-10	$\simeq$ 2'732	$\simeq$ 110
0.17	8.54e-11	$\simeq$ 5'908	$\simeq$ 236
0.15	7.53e-11	$\simeq$ 7'589	$\simeq$ 304
0.1	5.02e-11	$\simeq$ 17'074	$\simeq$ 683

In conclusion, performing a trade-off between accuracy, availability of computing power, and time, a proper number of simulations would be $n = 6'000$, resulting in about 4 hours of simulation time for each batch.

List of abbreviations and acronyms

APT Acoustic Power Transfer.

CPT Capacitive Power Transfer.

DIPS Differential Inductive Positioning System.

ED Equal Displacement.

EMC Electromagnetic Compatibility.

EMF Electric and Magnetic fields.

EVs Electric vehicles.

FCB Flight Controller Board.

FD Fixed Displacement.

FEMM Finite Element Method Magnetics.

FF Form factor.

FHA First Harmonic Approximation.

FS Firing Signal.

FWR Full Wave Rectifier.

GaN Gallium Nitride.

HPED Half Period Equal Displacement.

IEC International Electrotechnical Commission.

IoT Internet of Things.

IPT Inductive Power Transfer.

ISO International Organization for Standardization.

LCC inductance-capacitance-capacitance.

LCL inductance-capacitance-inductance.

Li-Ion Lithium Ion.

Li-Po Lithium Polymer.

LoS Line of Sight.

LPT Laser Power Transfer.

MOSFET Metal-Oxide-Semiconductor Field-Effect Transistor.

ND No Displacement.

NLoS Non Line of Sight.

OLoS Obstructed Line of Sight.

PDF Probability Density Function.

PP Parallel-Parallel.

PS Parallel-Series.

PSI Phase Shifting Index.

PWM Pulse Width Modulation.

Re Receiver.

RF Ripple factor.

RFPT Radio frequency Power Transfer.

SAE Society of Automotive Engineers.

SiC Silicon Carbide.

SMOP Single Module Output Power.

SoC State of Charge.

SP Series-Parallel.

SS Series-series.

SS-IPT Series-Series Compensated IPT.

THD Total Harmonic Distortion.

Tr Transmitter.

UAVs Unmanned Aerial Vehicles.

WPC Wireless Power Consortium.

WPT Wireless Power Transfer.

WSNs Wireless Sensor Networks.

List of Figures

List of Tables

Bibliography

[1] "A new plan for europe's sustainable prosperity and competitiveness, european commission https://commission.europa.eu/priorities-2024-2029/competitiveness."

[2] T. Ojha, T. P. Raptis, A. Passarella, and M. Conti, "Wireless power transfer with unmanned aerial vehicles: State of the art and open challenges," *Pervasive and Mobile Computing*, vol. 93, p. 101820, 2023.

[3] Z. Yang, W. Xu, and M. Shikh-Bahaei, "Energy efficient uav communication with energy harvesting," *IEEE Transactions on Vehicular Technology*, vol. 69, no. 2, pp. 1913–1927, 2020.

[4] C. Zhao, X. Li, and Y. Yao, "Quality analysis of battery degradation models with real battery aging experiment data," in *2023 IEEE Texas Power and Energy Conference (TPEC)*, pp. 1–5, 2023.

[5] C. Stöcker, R. Bennett, F. Nex, M. Gerke, and J. Zevenbergen, "Review of the current state of uav regulations," *Remote Sens.*, vol. 9, p. 459, May 2017.

[6] Z. Liu, T. Li, S. Li, and C. C. Mi, "Advancements and challenges in wireless power transfer: A comprehensive review," *Nexus*, vol. 1, no. 2, p. 100014, 2024.

[7] J. Van Mulders, D. Delabie, C. Lecluyse, C. Buyle, G. Callebaut, L. Van der Perre, and L. De Strycker, "Wireless power transfer: Systems, circuits, standards, and use cases," *Sensors*, vol. 22, no. 15, 2022.

[8] W. C. Brown, "The history of wireless power transmission," *Solar Energy*, vol. 56, no. 1, pp. 3–21, 1996. Wireless Power Transmission.

[9] M. Faraday, *Experimental researches in electricity*, vol. 122. Philosophical Transactions of the Royal Society of London, 1832.

[10] J. C. Maxwell, "A treatise on electricity and magnetism," *Oxford, Clarendon press*, 1873.

[11] N. Tesla, "World system of wireless transmission of energy," *Telegraph and Telephone Age*, 1927.

[12] N. Tesla, "Apparatus for transmission of electrical energy," *US Patent 649,621*, May 15 1900.

[13] "Wireless power consortium qi's official website, https://www.wireless powerconsortium.com /standards/qi-wireless-charging/."

[14] "Airfuel alliance resonant's official website, https://airfuel.org/airfuel-resonant/."

[15] "Airfuel alliance rf's official website, https://airfuel.org/airfuel-rf/."

[16] "Society of automotive engineers j2954 standard's official website, https://www.sae.org/standards/content/j2954_202408/."

[17] "International electrotechnical commission 61980-1 standard's official website, https://webstore.iec.ch/en/publication/31657."

[18] "International electrotechnical commission 61980-2 standard's official website, https://webstore.iec.ch/en/publication/66046."

[19] "International electrotechnical commission 61980-3 standard's official website, https://webstore.iec.ch/en/publication/66059."

[20] M. Hassanalian and A. Abdelkefi, "Classifications, applications, and design challenges of drones: A review," *Progress in Aerospace Sciences*, vol. 91, pp. 99–131, 2017.

[21] "Pro vector artist, https://www.shutterstock.com/g/provectorportfolio."

[22] A. Niccolai, A. Gandelli, F. Grimaccia, R. Zich, and S. Leva, "Overview on photovoltaic inspections procedure by means of unmanned aerial vehicles," in *2019 IEEE Milan PowerTech*, pp. 1–6, 2019.

[23] G. Bogel, L. Cousin, N. Iversen, E. S. M. Ebeid, and A. Hennig, "Drones for inspection of overhead power lines with recharge function," pp. 497–502, 08 2020.

[24] R. I. Mukhamediev, K. Yakunin, M. Aubakirov, I. Assanov, Y. Kuchin, A. Symagulov, V. Levashenko, E. Zaitseva, D. Sokolov, and Y. Amirgaliyev, "Coverage path planning optimization of heterogeneous uavs group for precision agriculture," *IEEE Access*, vol. 11, pp. 5789–5803, 2023.

[25] M. Asad, O. A. Aidaros, R. Beg, M. A. Dhahri, S. A. Neyadi, and M. Hussein, "Development of autonomous drone for gas sensing application," in *2017 International Conference on Electrical and Computing Technologies and Applications (ICECTA)*, pp. 1–6, 2017.

[26] B. X. Nguyen, W. Peng, and D. M. Vilathgamuwa, "An overview of power circuit topologies for inductive power transfer systems," in *2016 IEEE International Conference on Sustainable Energy Technologies (ICSET)*, pp. 256–263, 2016.

[27] V. Cirimele, "Design and integration of a dynamic ipt system for automotive applications," 2017.

[28] V. Shevchenko, O. Husev, R. Strzelecki, B. Pakhaliuk, N. Poliakov, and N. Strzelecka, "Compensation topologies in ipt systems: Standards, requirements, classification, analysis, comparison and application," *IEEE Access*, vol. 7, pp. 120559–120580, 2019.

[29] M. Z. Erel, K. C. Bayindir, M. T. Aydemir, S. K. Chaudhary, and J. M. Guerrero, "A comprehensive review on wireless capacitive power transfer technology: Fundamentals and applications," *IEEE Access*, vol. 10, pp. 3116–3143, 2022.

[30] C. Lecluyse, B. Minnaert, and M. Kleemann, "A review of the current state of technology of capacitive wireless power transfer," *Energies*, vol. 14, no. 18, 2021.

[31] J. Dai and D. C. Ludois, "A survey of wireless power transfer and a critical comparison of inductive and capacitive coupling for small gap applications," *IEEE Transactions on Power Electronics*, vol. 30, no. 11, pp. 6017–6029, 2015.

[32] "Dji's official website, https://www.dji.com/."

[33] "Parrot's official website, https://www.parrot.com/en."

[34] "Freefly's official website, https://freeflysystems.com/."

[35] "Fimi's official website, https://www.fimi.com/."

[36] "Yuneec's official website, https://shop.yuneec.com/eu."

[37] M. Hassanalian and A. Abdelkefi, "Classifications, applications, and design challenges of drones: A review," *Progress in Aerospace Sciences*, vol. 91, pp. 99–131, 2017.

[38] V. Cirimele, R. Mandrioli, R. Torchio, G. Gentile, F. Giulietti, and G. Grandi, "Design considerations on modular wpt charging systems for drones in civil applications," in *2023 International Conference on Clean Electrical Power (ICCEP)*, pp. 452–457, 2023.

[39] F. Grazian, T. B. Soeiro, and P. Bauer, "Design trade-offs between the coupled coils' inductance and the series-series compensation capacitance for ev wireless charging systems," in *Proc. Int. Symp. Power Electron., Electr. Drives, Autom. Motion (SPEEDAM)*, (Sorrento, Italy), pp. 270–276, 2022.

[40] J. Boys, G. Covic, and A. W. Green, "Stability and control of inductively coupled power transfer systems," *Proc. IEE–Elect. Power Applicat.*, vol. 147, pp. 37–43, Jan. 2000.

[41] "Laird ferrite disk vendor's page. https://www.mouser.it/productdetail/laird-technologies/mm1400-300?qs=p6tritwzfmxxsyvmftpfcw

[42] "Kemet ferrite parallelepiped vendor's page. https://www.mouser.it/productdetail/kemet/fpl100-100-4-bh1t?qs=

[43] "Block cul 500/1,00 vendor's page. https://www.block.eu/en_en/productversion/cul-500100."

[44] "Bq dn2e 1.00 vendor's page. https://shop.darisusgmbh.de/en/cable/wires/transformer-winding-wires/dn2e1-00-0-25-coil-wire-enamelled-dn2e-200-grad-c-dia-1-00mm-0-25kg-35m::32543.html."

[45] "Würth elektronik's official website, https://www.we-online.com/de."

[46] "Tdk's official website, https://www.tdk.com/en/index.html."

[47] "Signal bel's official website, https://www.belfuse.com/company/brands/signal-transformer."

[48] "Vishay's official website, https://www.vishay.com/."

[49] "Finite element method magnetics (femm) documentation, https://www.femm.info/wiki/documentation/."

[50] T. Boulanger, V. Cirimele, M. Ricco, and E. Monmasson, "Z-specnnet: A real-time embedded nn-based parameters estimation for wpt systems," *IEEE Transactions on Industrial Electronics*, vol. 72, no. 7, pp. 7595–7604, 2025.

[51] C.-S. Wang, G. Covic, and O. Stielau, "Power transfer capability and bifurcation phenomena of loosely coupled inductive power transfer systems," *Industrial Electronics, IEEE Transactions on*, vol. 51, pp. 148 – 157, 03 2004.

[52] V. Cirimele, R. Torchio, J. L. Villa, F. Freschi, P. Alotto, L. Codecasa, and L. D. Rienzo, "Uncertainty quantification for sae j2954 compliant static wireless charge components," *IEEE Access*, vol. 8, pp. 171489–171501, 2020.

[53] "Kemet corporation. capacitor selection guide. https://www.filcap.de/wp-content/uploads/gesamtkatalog-kemet-capacitor-selection-guide.pdf."

[54] "Alcon electronics. general purpose film capacitors datasheet ff 12. https://alconelectronics.com/wp-content/uploads/2019/11/general-purpose-film-capacitors-datasheet-ff-12.pdf."

[55] "Ieee standard for the design of chargers used in stationary battery applications," *IEEE Std 2405-2022*, pp. 1–48, 2022.